

Contents lists available at [ScienceDirect](https://www.sciencedirect.com)

International Journal of Applied Earth Observations and Geoinformation

journal homepage: www.elsevier.com/locate/jag

Joint use of Sentinel-2 and Sentinel-1 data for rapid mapping of volcanic eruption deposits in Southeast Asia

Aiym Orynbaikyzy^{a,*}, Simon Plank^a, Yenni Vetrira^b, Sandro Martinis^a, Imam Santoso^b, Rido Dwi Ismanto^b, Farikhotul Chusnayah^b, Arum Tjahjaningsih^b, Suwarsono^b, Nicola Genzano^c, Francesco Marchese^d, M. Rokhis Khomarudin^b, Günter Strunz^a

^a German Remote Sensing Data Center (DFD), German Aerospace Center (DLR), Muenchner Strasse 20, 82234 Wessling, Germany

^b Research and Innovation Agency (BRIN), Research Center for Remote Sensing, Jl. Lapan No. 70, Pekayon Pasar Rebo, Jakarta 13710, Indonesia

^c University of Basilicata, School of Engineering, Via dell'Ateneo Lucano, 85100 Potenza, Italy

^d National Research Council, Institute of Methodologies for Environmental Analysis, C. da S. Loja, 85050 Tito Scalco (Pz), Italy

ARTICLE INFO

Keywords:

Rapid mapping
Change detection
Volcano hazards
Region growing
Sentinel-1
Sentinel-2

ABSTRACT

Indonesia and Papua New Guinea (PNG) have 97 active volcanoes with high concentration of human life in the very close proximity to them. In case of a volcanic eruption, provision of detailed information on affected regions is very crucial to support rescue and humanitarian relief organizations. In this paper, we present a semi-automated unsupervised knowledge-based region growing procedure that utilizes Synthetic Aperture Radar (SAR) data, from Sentinel-1, and optical data, from Sentinel-2, for mapping land surface changes after volcanic eruptions. With initial seed points, being placed on active volcano vents and areas affected by thermal anomalies (derived from Sentinel-2), the region growing procedure considers interferometric coherence data in unvegetated sites, and radar brightness and polarimetric decomposition features at vegetated sites. We selected five eruptive events that occurred between 2018 and 2021 at the Indonesian volcanoes of Karangetang, Semeru, Sinabung and at Ulawun Volcano on PNG. The eruption patterns varied with respect to duration, spatial extent and ejected volcanic materials. The results indicated that usage of radar brightness features with interferometric coherence already gives good change delineation. However, in the Ulawun test case, where heavy ash and scoria fall occurred, the addition of polarimetric decomposition features substantially improved the output accuracy due to the improved detection of ash deposits. The presented change detection method is straight forward to implement, and will strongly improve rapid mapping activities during as well as after major volcano eruptions.

1. Introduction

Volcanic eruptions, depending on the volcanic explosivity index (VEI), can have devastating impact on human lives and disrupt human livelihoods. With the growing concentration of critical infrastructure (e. g., submarine communication cables, power plants) and human population around active volcanoes (Fig. 1), the lower magnitude volcano eruptions $VEI \leq 3$ would become more hazardous than before (Mani et al., 2021). Despite the scientific effort to predict the timing of volcano activity, many major eruptions occur unexpected even at well monitored volcanoes (Barclay et al., 2019). In such a scenario, acquiring the information on the spatial extent of the hazard area is vital for planning and execution of effective and timely followed first response actions.

Acquiring ground-based information or aerial imagery from active

hazard zones is often hardly possible. In that respect, satellite remote sensing has a unique position by offering time relevant, large-scale, regular information over the area of interest from space that enables monitoring of the volcanic eruption without imposing danger to human lives (Cigna et al., 2020).

During a volcanic eruption, the land surface change normally occurs due to the ejected volcano materials such as lava flows, pyroclastic density currents (PDC), primary lahars, volcanic debris avalanches and heavy ashfall. Here, by change we imply a long- or short-term transition of a pre-eruption land cover land use (LCLU) class to one of the above-mentioned post-eruption volcanic deposits classes. Mapping of such changes, within remote sensing domain, is normally performed using change detection techniques (Hechteltjen et al., 2014).

Optical and Synthetic Aperture Radar (SAR) data are the most widely

* Corresponding author.

E-mail address: aiym.orynbaikyzy@dlr.de (A. Orynbaikyzy).

<https://doi.org/10.1016/j.jag.2022.103166>

Received 4 October 2022; Received in revised form 9 December 2022; Accepted 17 December 2022

Available online 20 December 2022

1569-8432/© 2022 The Authors. Published by Elsevier B.V. This is an open access article under the CC BY-NC-ND license (<http://creativecommons.org/licenses/by-nc-nd/4.0/>).

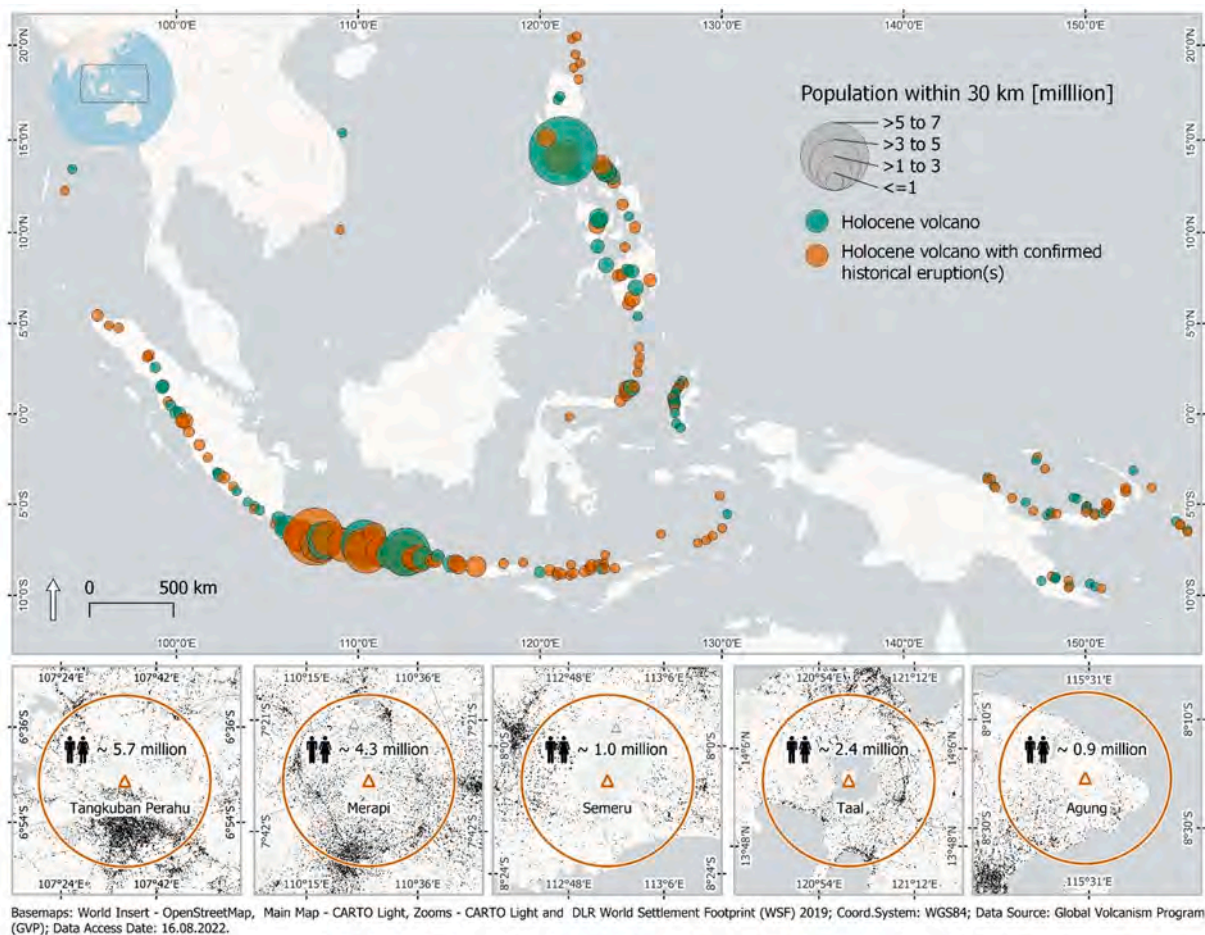


Fig. 1. Human population within 30 km distance (where large portion of fatalities occur (Auker et al., 2013)) from an active volcanoes in southeast Asia and Papua New Guinea (top). The zoomed view on five volcanoes (bottom) provide more details on the number of people and spatial distribution of settlements (Marconcini et al., 2021).

used remote sensing datasets for volcano monitoring and post disaster impact assessment. Since affected areas from inland volcano hazards normally cover small area in the close proximity to the volcanoes, optical data are often used for visual interpretation and manual delineation of changes (e.g., De Beni et al., 2021; Pallister et al., 2019). Semi-automated solutions were presented in recent studies for mapping volcanic deposits with very high and high spatial resolution optical data (Corradino et al., 2019; Rösch and Plank, 2022). However, utility of optical data suffers when the spectral response over changed sites does not contrast from the background or the information on optical data is disrupted due to the presence of clouds, cloud shadows or ash plumes (Aldeghi et al., 2019). In that respect, SAR data have clear advantages with its all-weather image sensing capabilities as well as by providing useful information independently of the sunlight.

The post-eruption change detection using SAR data mainly relies on interferometric coherence and radar intensity information. Interferometric coherence, as a by-product of the Interferometric SAR (InSAR) technique, is extensively used for change detection on unvegetated volcano flanks (e.g., Bignami et al., 2020; Joyce et al., 2009; Jung et al., 2016). However, its application over vegetated sites is limited due to the constant vegetation motion that causes the loss of coherence (Dietterich et al., 2012). The usage of the variation of radar intensities between pre- and post-eruption scenes (e.g., Bignami et al., 2020; Solikhin et al., 2015) or manual delineation of disrupted vegetation using optical data (e.g., Smets et al., 2010) is used in the literature to overcome this issue. While usage of interferometric coherence and radar intensity for mapping volcano deposits is well established in the literature, the

application of polarimetric decomposition features is rarely addressed despite its proven effectiveness in, for instance, mapping flooded vegetation (Brisco et al., 2013) or detecting landslide area (Plank et al., 2016).

In this study, we propose an unsupervised, knowledge-based seeded region growing method for land surface change detection after volcanic eruptions using freely available Sentinel-1 and Sentinel-2 data. We also test the utility of polarimetric decomposition features together with radar brightness information for mapping changes on vegetated areas. With the hypothesis that the usage of more than one pre-event scene for image difference calculation could reduce the noise in SAR data and lead to better accuracies, we examine accuracies acquired based on features calculated using one and five pre-event scenes. The workflow is straight forward to replicate and can be used for rapid change detection tasks for volcanoes in southeast Asia.

2. Study sites and test cases

We selected five recent volcanic activities that occurred between 2018 and 2021 at three Indonesian (Karanteng, Semeru, Sinabung) and one Papua New Guinean (Ulawun) volcanoes (Fig. 2). Indonesia and Papua New Guinea are among the top five countries in the expected fatality rate risk from volcano induced hazards (Pan et al., 2015) due to frequent eruption patterns and dense human concentration around active volcanoes. Also, as topical countries, they have higher probability of experiencing primary lahars, that together with PDCs are the main causes of direct fatalities from volcanic eruptions (Auker et al., 2013).

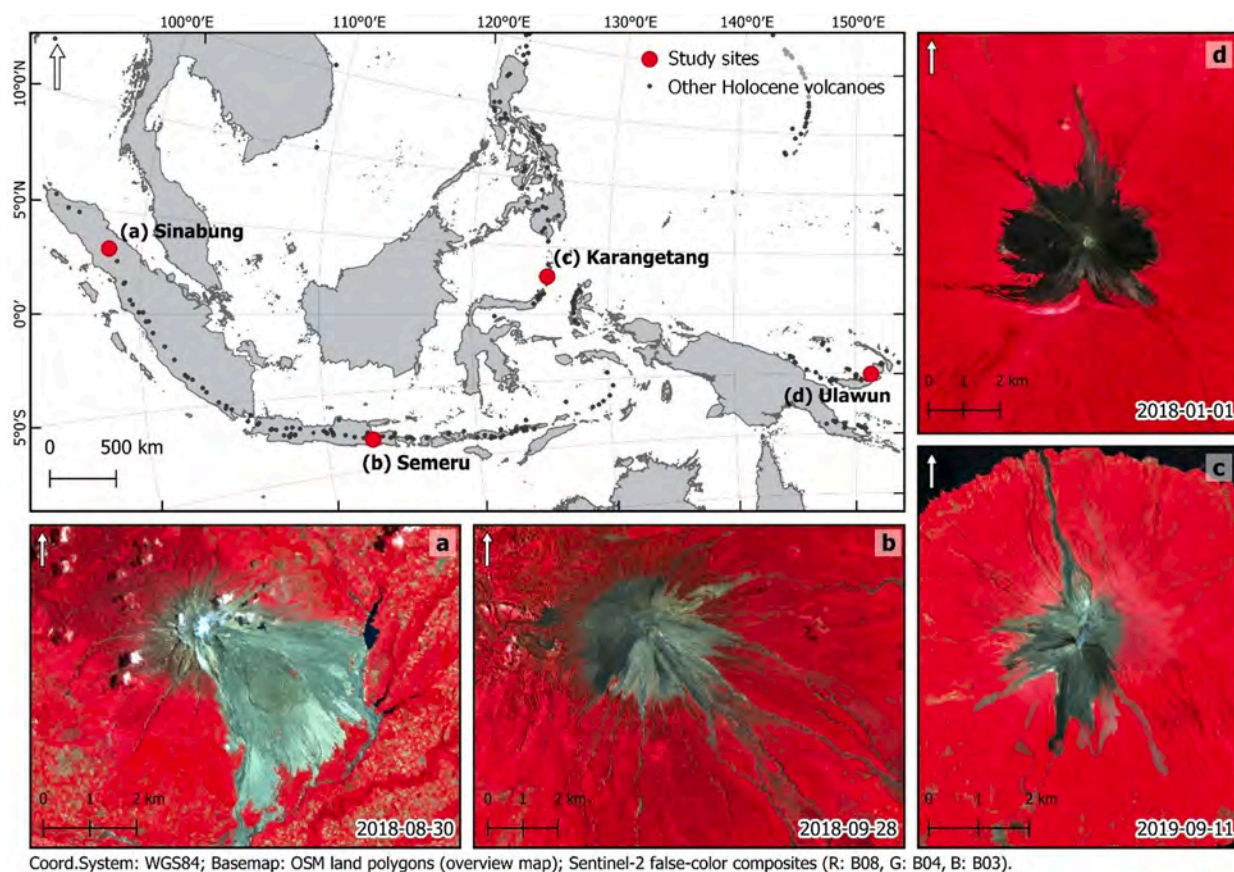


Fig. 2. Study sites in Indonesia (a. Sinabung, b. Semeru, c. Karangetang) and Papua New Guinea (d. Ulawun).

Table 1
Overview of Sentinel-2 satellite images used in this study.

Karangetang (N)	Karangetang (W)	Semeru	Sinabung	Ulawun
<i>NDVI comp.*:</i>	<i>NDVI comp.*:</i>	<i>NDVI comp.*:</i>	<i>NDVI comp.*:</i>	<i>NDVI comp.*:</i>
2018-09-01	2019-04-14	2021-09-07	2020-12-07	2019-04-06
2018-09-06	2019-04-24	2021-09-17	2020-12-27	2019-04-21
2018-09-11	2019-04-29	2021-09-22	2021-01-01	2019-04-26
2018-09-21	2019-05-04	2021-09-27	2021-01-11	2019-05-11
2018-09-26	2019-05-09	2021-10-02	2021-01-16	2019-05-16
2018-10-01	2019-05-14	2021-10-07	2021-02-05	2019-05-26
2018-10-06	2019-05-19	2021-10-12	2021-02-10	2019-05-31
2018-10-21	2019-05-24	2021-10-17	2021-02-15	2019-06-25
2018-10-31	2019-05-29	2021-10-22	2021-02-20	<i>Thermal anom.**:</i>
2018-11-05	2019-06-08	<i>Thermal anom.**:</i>	2021-02-25	No scenes
2018-11-10	2019-06-13	2021-12-06	<i>Thermal anom.**:</i>	
<i>Thermal anom.**:</i>	2019-06-23		2021-03-02	
37 scenes from 2018 to 11-20 until	2019-06-28			
2019-03-25	2019-07-03			
	<i>Thermal anom.**:</i>			
	47 scenes from 2019 to 07-13 until			
	2020-02-28			

* NDVI comp. – NDVI composite;

** Thermal anom. – thermal anomalies.

The considered eruption events substantially differ in their duration, ejected volcanic materials and spatial extent. In the following sub-chapters, more in depth description of the considered events are given.

2.1. Karangetang (Indonesia)

Karangetang (Api Siau) is an active stratovolcano, located on Siau Island in Indonesia with the peak reaching 1,827 m. It is one of the most

active volcanoes of the country.

We examine two recent eruptions that produced ash plumes, small-scale PDCs and lava flows. In both activities, lava flows were the main cause for the land cover change on the volcano flanks. The first event started at the end of November 2018. The first volcanic thermal anomalies, which were identified by the MODVOLC algorithm (Wright et al., 2004) analysing thermal imagery of MODIS in near-real-time, were detected on 24th of November after increased seismicity in

Table 2
Overview of Sentinel-1 satellite images used in this study.

Karanteng (N)		Karanteng (W)				Semeru		Sinabung		Ulawun	
date	*rel. orbit	date	*rel. orbit	date	*rel. orbit	date	*rel. orbit	date	*rel. orbit	date	*rel. orbit
2018-10-07	163 ¹	2019-05-23	163 ¹	2021-10-08	54 ²	2021-01-29	143 ²	2019-05-05	67 ²		
2018-10-19		2019-06-04		2021-10-20		2021-02-04		2019-05-17			
2018-10-31		2019-06-16		2021-11-01		2021-02-10		2019-05-29			
2018-11-12		2019-06-28		2021-11-13		2021-02-16		2019-06-10			
2018-11-24		2019-07-10		2021-11-25		2021-02-28		2019-06-22			
2018-12-06		2019-07-22		2021-12-07		2021-03-06		2019-07-04			
2018-12-18		2019-08-03									
2018-12-30		2019-08-15									
2019-01-11		2019-08-27									
2019-01-23		2019-09-08									
2019-02-04		2019-09-20									
2019-02-16		2019-10-02									
2019-02-28		2019-10-14									
		2019-10-26									
		2019-11-19									
		2019-12-01									
		2019-12-13									
		2019-12-25									
		2020-01-18									
		2020-01-30									
		2020-02-11									
		2020-02-23									

* relative orbit.
¹ descending mode.
² ascending mode.

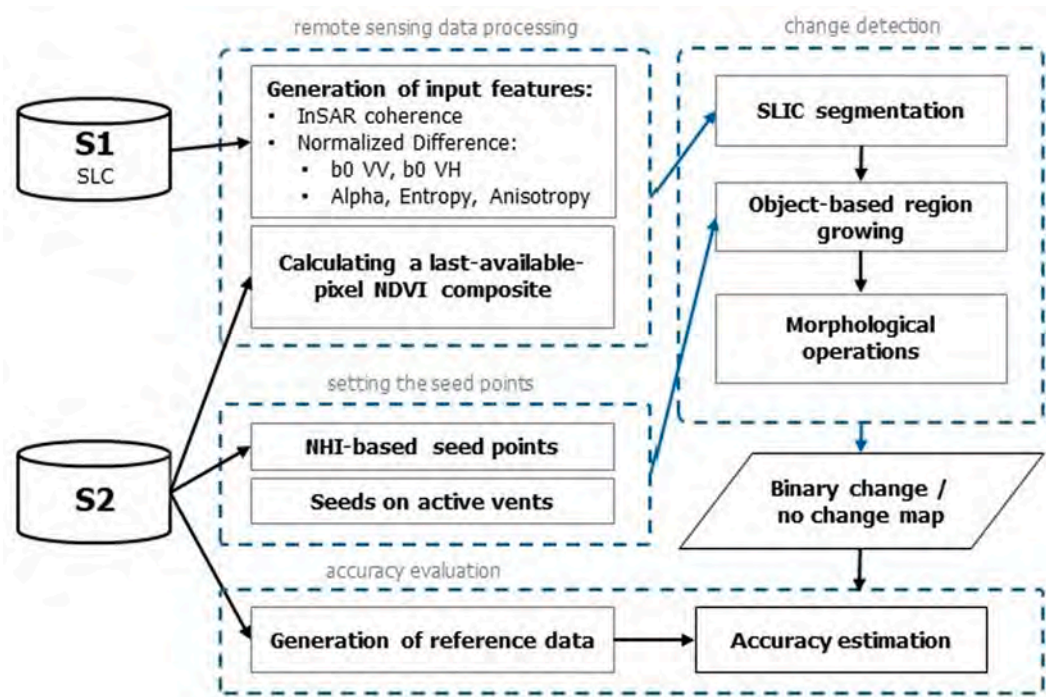


Fig. 3. Unsupervised, knowledge-based region growing workflow for detecting volcanism-related land surface changes.

previous days. The following lava flow extrusion from the northern crater (Kawah Dua) triggered small avalanches and pyroclastic flows. The lava flew towards north and small ash plumes continued until the end of March 2019. The flow covered the road that were connecting several communities on the island and entered the sea on 5th of February (Global Volcanism Program, 2019a).

The second eruption started on mid-July 2019 and continued until mid-January 2020 (Genzano et al., 2020). The increased thermal anomalies on the southern crater (Kawah Utama) followed by extrusion of incandescent avalanche blocks and lava flow on western side of the volcano flank. The incandescent blocks travelled down to 1000 – 1500 m along the multiple drainages (Global Volcanism Program, 2020). Sentinel-2 false colour composite image in Fig. 2.c illustrates land surface state of Karanteng during the second eruption event.

2.2. Semeru (Indonesia)

With its continuous activity since 1967, Semeru Volcano (Fig. 2.b, pre-event image) is known as one of the most hazardous and active volcanoes worldwide. Located on the world’s most populated island - Java, its explosive eruptions often result into the displacement of communities in the close proximity or event fatalities among them.

During several days of heavy rain, an explosion and a dome collapse on 4th of December 2022 produced a 15 km high ash plume and pyroclastic flow that generated lahars travelling down the Kobokan river towards southeast (Global Volcanism Program, 2022). This eruption could have been triggered by heavy rains that eroded the lava dome and lead to its collapse and consequent major explosion (Handley, 2021).

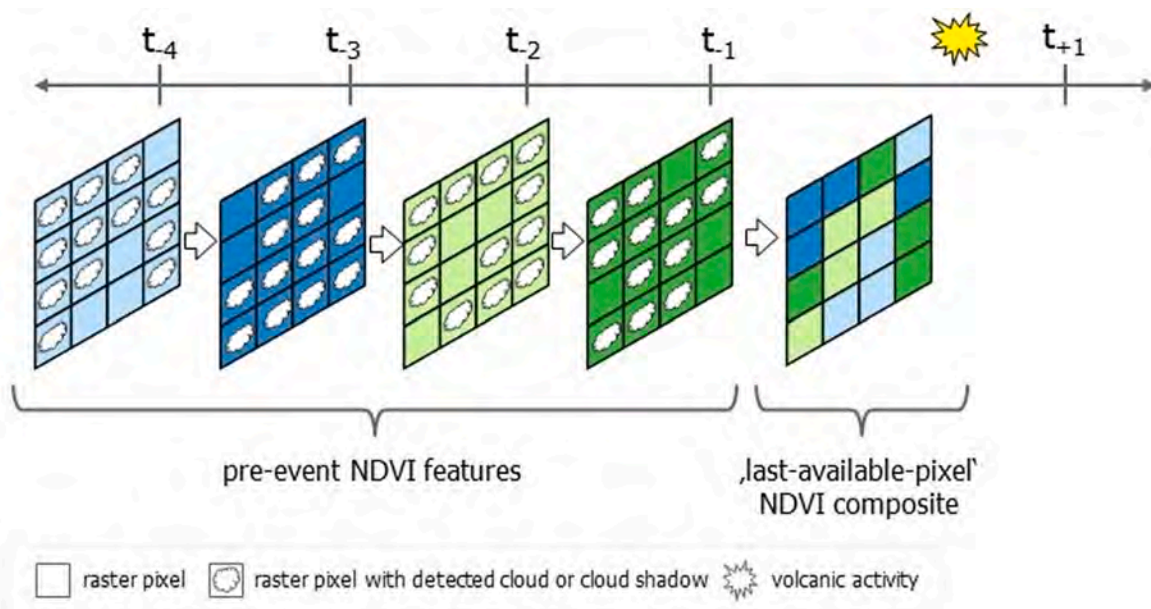


Fig. 4. Generation of 'last-available-pixel' NDVI composite.

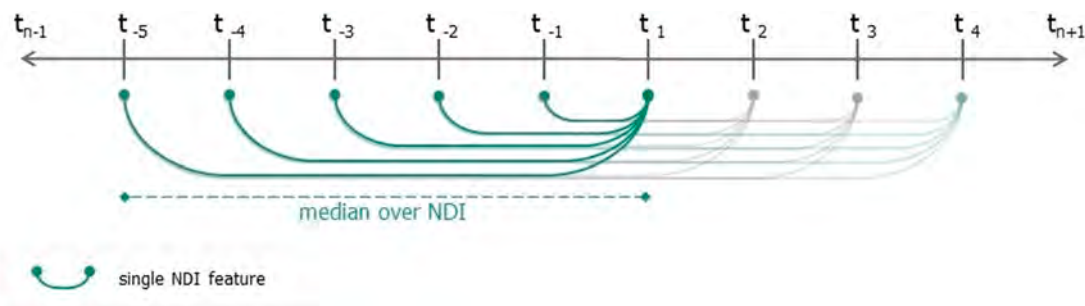


Fig. 5. Calculation of mNDI features.

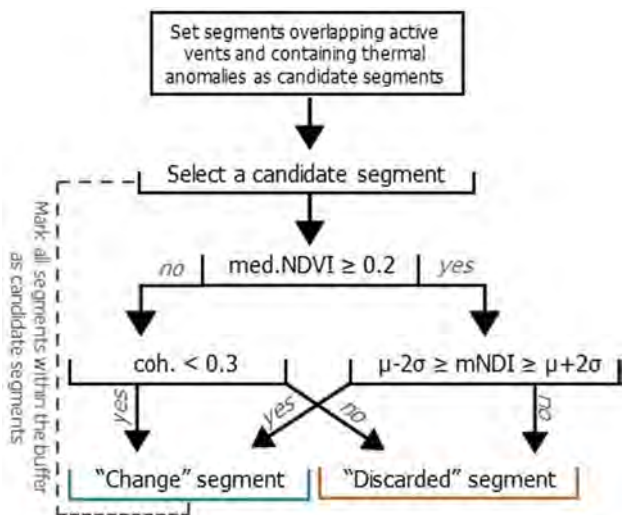


Fig. 6. Seeded region growing procedure.

2.3. Sinabung (Indonesia)

Located on the northern part of Sumatra Island, Sinabung had its first confirmed Holocene eruption in 2010. The elongated stratovolcano had

several activity phases since 2010 which included lava flows, pyroclastic flows, block avalanches and explosions with ash plumes (Fig. 2.a, pre-event image).

The considered activity started in the early morning on 2nd of March 2021. According to the report from Center of Volcanology and Geological Hazard Mitigation (CVGHM, also known as PVMBG), 15 pyroclastic flows and ash plumes with the height of 12.2 km were recorded on that day. The pyroclastic flows and block avalanches travelled down the east and south east direction up to 3.7 km (Global Volcanism Program, 2021).

2.4. Ulawun (Papua New Guinea)

The highest volcano (2334 m) on Bismarck Archipelago – Ulawun (Fig. 2.d, pre-event image), is one of the most active volcanoes of Papua New Guinea. The volcano is located on the north-eastern part of New Britain Island. Several large eruptions after 1970 generated pyroclastic and lava flows.

On 26th of June 2019, the sharply increased seismicity was the precursor of the eruption that started at early morning with grey ash plume. Ash plumes that rose above 8 and 13 km drifted in west, south and south-eastern directions and caused substantial amounts of ashfall. The lava or pyroclastic flows were reported to reach some of the villages around the volcano (Global Volcanism Program, 2019b). No fatalities were reported but the eruption forced around 11,000 people flee their homes. The heavy ash fall damaged several main roads, houses and

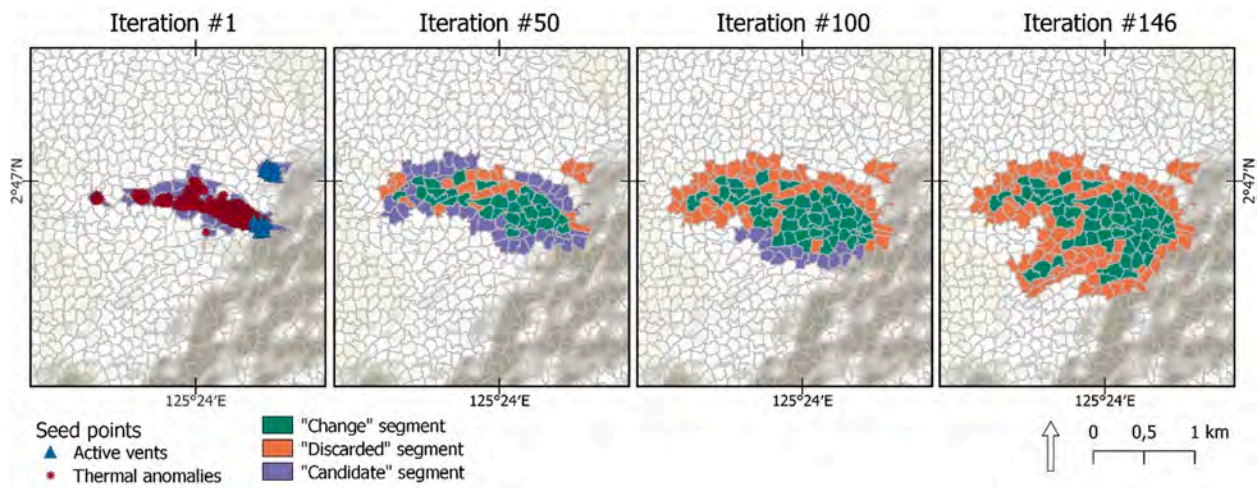


Fig. 7. Example of region growing iterations of Karangetang (W) test case.

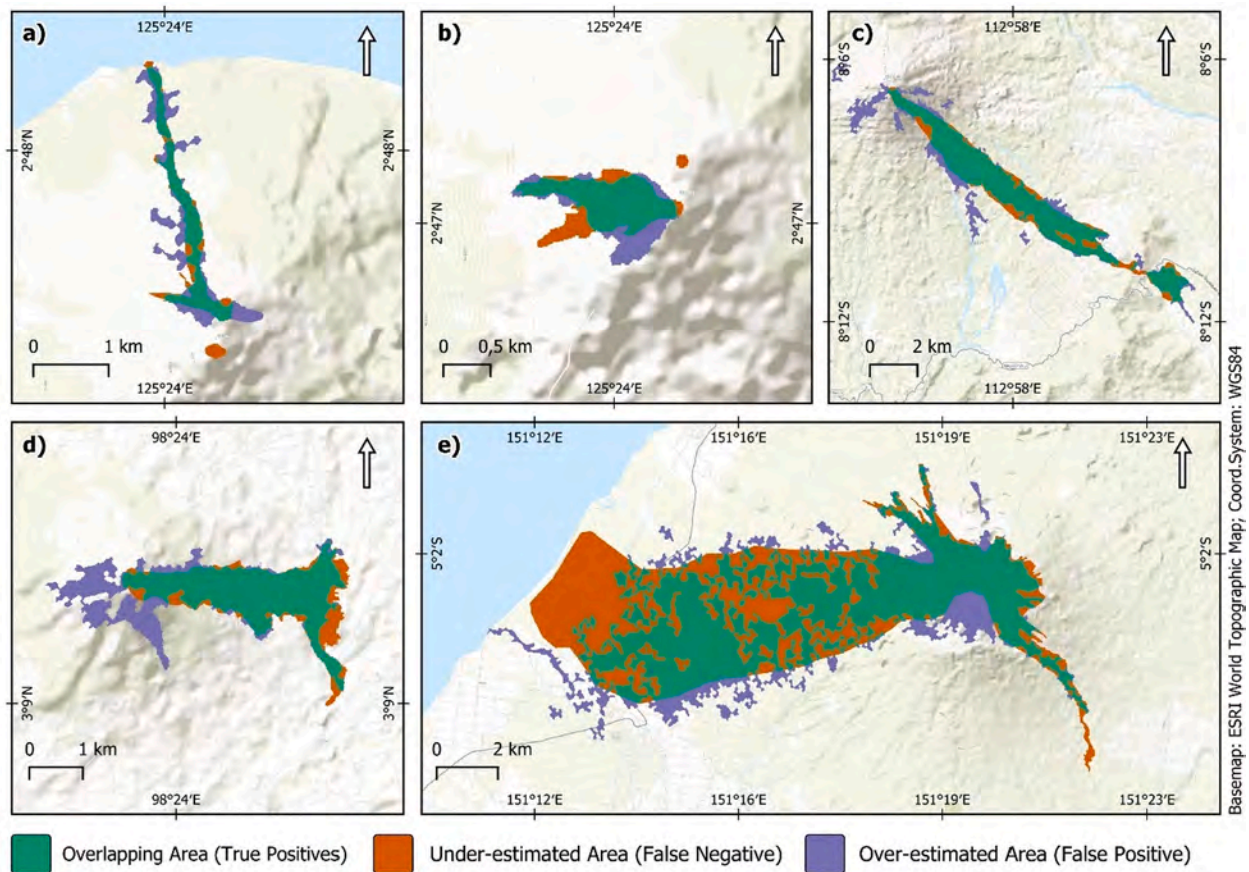


Fig. 8. Area-based change detection results using combination of radar brightness and polarimetric decomposition features for test cases in a) Karangetang (N) on 16 February 2019, b) Karangetang (W) on 23 February 2020, c) Semeru, d) Sinabung and c) Ulawun.

schools (Bevege, 2019).

3. Remote sensing data and its Pre-Processing

Optical data from Sentinel-2 A/B and SAR data from Sentinel-1 A/B satellites were used for the analysis. Sentinel satellites launched within European Space Agency’s (ESA) Copernicus program, provide freely accessible high spatial and temporal resolution images at global scale. Remote sensing images from both satellites were directly downloaded

from the Copernicus Open Access Hub (URL:).

In total, 52 Sentinel-2 A/B images with cloud cover less than 80 % were acquired for building cloud-free Normalized Difference Vegetation Index (NDVI) composites (Table 1). For constructing the pre-event cloud-free NDVI composites we used the images acquired within last 90 days before the start of the considered eruption event. The range of 90 days was selected empirically based on the quality of output cloud-free composites. The threshold was raised up to 120 days for Ulawun, due to the absence of sufficient amount of clear sky data. All Sentinel-2

Table 3
Area-based accuracy estimation results.

	VV,VH + H/A/α				VV,VH				H/A/α			
	I*		5*		I*		5*		I*		5*	
	IoU	Dice	IoU	Dice	IoU	Dice	IoU	Dice	IoU	Dice	IoU	Dice
Karangetang (N) ¹	0.44	0.61	0.46	0.63	0.45	0.62	0.52	0.69	0.32	0.49	0.44	0.61
Karangetang (W) ²	0.55	0.71	0.56	0.72	0.56	0.72	0.58	0.74	0.51	0.68	0.54	0.70
Semeru	0.57	0.73	0.63	0.77	0.56	0.72	0.63	0.78	0.30	0.46	0.33	0.50
Sinabung	0.56	0.72	0.58	0.74	0.60	0.75	0.58	0.74	0.56	0.71	0.56	0.72
Ulawun	0.47	0.64	0.53	0.69	0.24	0.39	0.31	0.47	0.36	0.53	0.46	0.63

* number of pre-event scenes;

¹ accuracies calculated based on detected changes on 16th of February. 2019;

² accuracies calculated based on detected changes on 23rd of February 2020.

Table 4
Point-based accuracy estimation results.

	VV,VH + H/A/α		VV,VH		H/A/α	
	I*	5*	I*	5*	I*	5*
	F1-score	F1-score	F1-score	F1-score	F1-score	F1-score
Karangetang (N) ¹	0.88	0.91	0.77	0.90	0.65	0.81
Karangetang (W) ²	0.86	0.87	0.86	0.86	0.79	0.82
Semeru	0.82	0.92	0.80	0.89	0.46	0.49
Sinabung	0.89	0.87	0.88	0.85	0.82	0.83
Ulawun	0.57	0.68	0.20	0.32	0.42	0.61

* number of pre-event scenes.

¹ accuracies calculated based on detected changes on 16th of February. 2019;

² accuracies calculated based on detected changes on 23rd of February 2020.

images were pre-processed from Level-1C Top-of-Atmosphere to Level-2A Bottom-of-Atmosphere products using Sen2Corr (v 2.10). NDVI bands were then calculated using red (B4) and near-infrared bands (B8) for each optical image.

Optical data for detecting thermal anomalies were directly accessed via Google Earth Engine platform (GEE) and run through the Normalized Hotspot Indices (Marchese et al., 2019) tool (Genzano et al., 2020) (available online at <https://nicogenzano.users.earthengine.app/view/nhi-tool>). The Sentinel-2 A/B Level-1C data sensed during each eruption activity were used as input.

For each test case we acquired Sentinel-1 A/B Interferometric Wide (IW) swath, Single Look Complex (SLC) scenes covering the activity period and five pre-event scenes (Table 2). The pre-processing of Sentinel-1 data was done using Sentinel-1 Toolbox (S1TBX) executed using the Graph Processing Tool of the Sentinel Application Platform (SNAP) software (v 8.0).

4. Methodology

4.1. General workflow

In southeast Asia, the flanks of volcanoes are typically densely vegetated. The unvegetated sites often appear on craters above active vents or where vegetation was disrupted due to the previous effusive or explosive eruptions. While interferometric coherence is a reliable measure of change on non-vegetated surfaces (Tzouvaras et al., 2020), it has less utility for detecting changes on vegetated sites due to constant motion of vegetated surfaces. Disruption of dense vegetation by lava flows, PDCs or lahars would lead to substantial alteration of surface roughness and its dielectric properties that could be captured by radar intensity or polarimetric decomposition features. Considering this, we set up the change detection workflow that uses the most suitable input features for each location, vegetated and unvegetated. The workflow consists of three main steps: generation of input features, super-pixel

segmentation and seeded region growing (Fig. 3).

4.2. Generation of input features

4.2.1. NDVI 'last-available-pixel' composite

To separate vegetated from non-vegetated sites we calculated a pre-event NDVI last-available-pixel composite. The NDVI composite was calculated using the linear forward interpolation of valid NDVI values to the last pre-event NDVI layer (Fig. 4). The validity of pixels was defined by the quality mask that combined information from cloud probability layers and cloud-shadow masks. We used the Sentinel-2 cloud probability data, accessed via GEE platform (Gorelick et al., 2017), which was previously reported to perform similar or even better than other state-of-the-art cloud detection tools (López-Puigdollers et al., 2021). The cloud shadow detection was done using the intersection of cloud shadow projection with dark near-infrared pixels that is not water (Braaten, 2022). Pixels that had cloud probability of 40 % or were marked as cloud shadow were labelled as invalid pixels in the quality mask. The lower cloud probability threshold was set to avoid under-detection of clouds that could substantially worsen the quality of output NDVI composite.

4.2.2. Interferometric coherence

For mapping changes on unvegetated surfaces we calculated interferometric coherence layers using the two temporally adjacent complex SAR scenes. The coherence layers range from 0 to 1 and describe the similarity of the reflected radar backscatter between two scenes acquired with the same imaging geometry over the same place but at difference time. Values closer to 1 indicate high similarity between the two scenes, whereas values closer to 0 indicate low similarity. Before calculating coherence layers, several pre-processing steps are required such as image calibration, co-registration, coherence calculation, debursting and terrain correction using Copernicus Digital Elevation Model (DEM) data.

For the events with a single large eruption (e.g., Semeru, Sinabung, Ulawun) we used co-event coherence layers that show low values over regions affected by the eruption of interest on unvegetated surfaces. For events that continued for several months (e.g., Karangetang (N), Karangetang (W)), the mean coherence values since the start of the respective event was used as an input. Towards the end of ejection of the volcanic materials, the coherence values over unvegetated sites would increase indicating the end of the active phase.

4.2.3. Radar brightness and polarimetric features

To map the changes on vegetated sites, we used radar brightness at the two polarizations VV and VH provided by Sentinel-1 and calculated polarimetric decomposition features. SAR data from Sentinel-1 A/B were radiometrically calibrated to Beta Naught (β_0) values using Copernicus DEM data, also called as radar brightness. Radar brightness values are independent from the terrain (yet the influence of incidence angle is still present) and represent the reflectivity per unit of area in slant range.

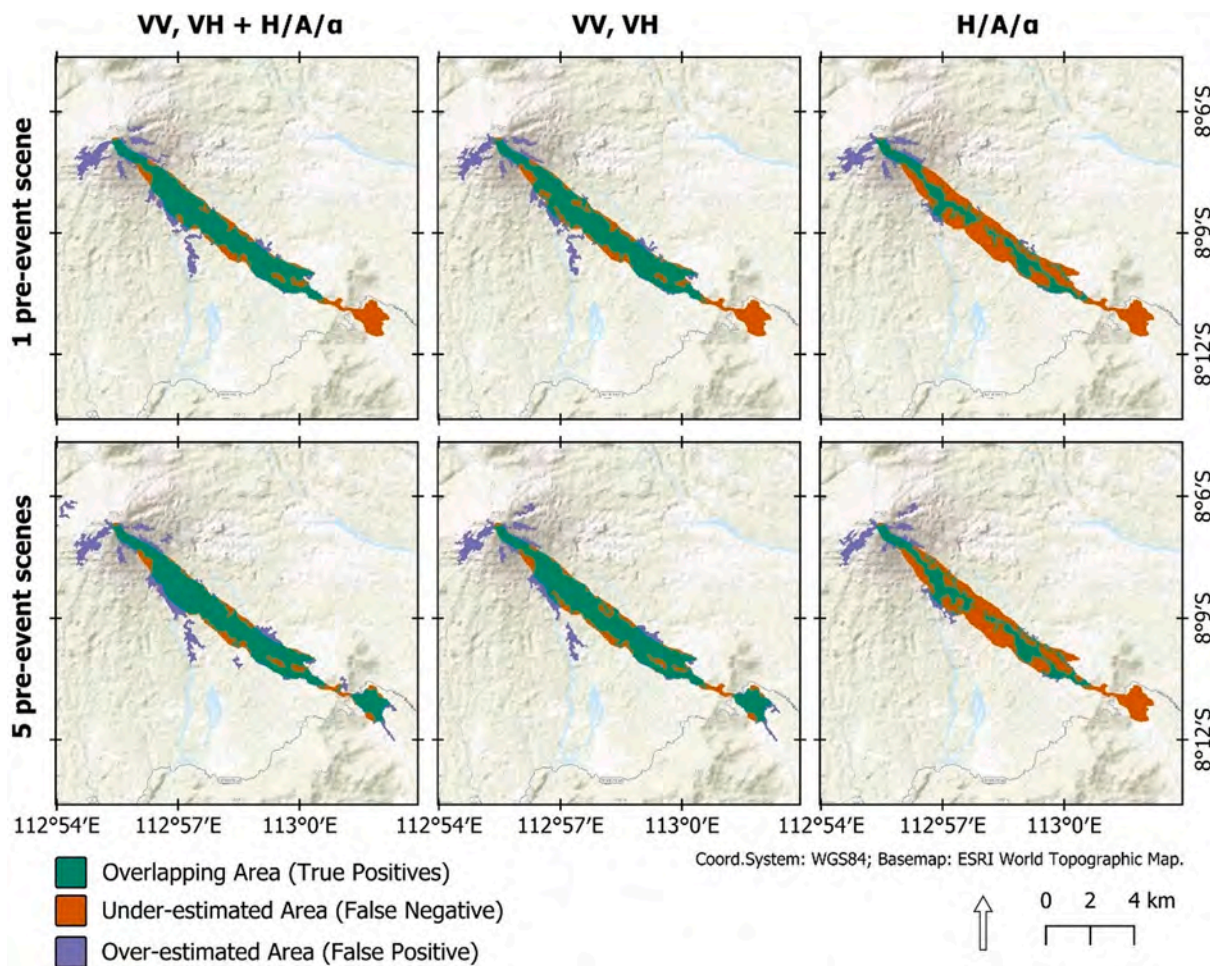


Fig. 9. Area-based change detection results using three features groups (columns) calculated based on one and five pre-event scenes (rows) for test case Semeru Volcano.

Additional to radar brightness, we explored the potential of using polarimetric SAR features for rapid mapping of land surface changes. Polarimetric SAR data that utilize the information on polarization state of emitted and received waves enable inferences on the properties of the targets on the ground. The changes of the wave polarization after the interaction with the target depend on the properties of the interacting surface (e.g., surface roughness, moisture content, reflectivity, orientation, structure). When the properties of the sensed surface change over time it leads to change on output polarimetric images.

The polarimetric decomposition allows to measure the relative contribution of scattering mechanisms that occur on the ground such as surface, volume, and double-bounce scattering. As Sentinel-1 acquires dual-pol data, we performed the dual-pol entropy(H)/anisotropy(A)/alpha(α) decomposition, developed by Cloude and Pottier (1997), that is based on eigenvalues of the covariance matrix C2 (Nielsen et al., 2017). Three parameters are given as an output of the H/A/ α decomposition – mean scattering alpha angle (α), polarimetric scattering entropy (H) and scattering anisotropy (A).

The alpha angle corresponds directly to the average scattering mechanism. The values vary from 0° to 90°, where values around 0 indicate surface scattering, around 45° volume scattering and around 90° the domination of double-bounce scattering. Entropy contains information about the heterogeneity of the scattering mechanism and vary from 0 to 1. Values closer to 0 imply domination of one scattering mechanism whereas those closer to 1 indicate complete random scattering. Anisotropy provide additional information to entropy and helps

to differentiate various types of surface scattering and its values vary from 0 to 1.

The radar brightness at the two polarizations (VV, VH) and three polarimetric decomposition features have different value ranges. To use these variables together and bring them into one value range we adopted a normalized difference index (NDI). With the aim of reducing the noise that could be the result of short-term atmospheric effects we calculate NDI with five pre-event scenes and took the median value (mNDI) (Fig. 5). Following equation was used for the calculating the

$$mNDI : mNDI = med. \left(\frac{pre - event - post - event}{pre - event + post - event} \right) \quad (1)$$

The values vary from -1 to 1, where values closer to 0 indicate no change and those further away from 0 would indicate strong increase or decrease of values in the post-event scene.

4.3. Super-Pixel segmentation

For segmenting the images we used scikit-image implementation (van der Walt et al., 2014) of the Simple Linear Iterative Clustering (SLIC) super-pixel algorithm (Achanta et al., 2012) in version 0.19. SLIC is a simple pixel clustering algorithm that reported to be fast and well performing with the minimal set of input parameters (Clauss et al., 2018). The two important parameters that could substantially affect the quality of the segmentation are the compactness and $n_segments$. After imperative evaluation of various parameters, we set compactness to 0.1

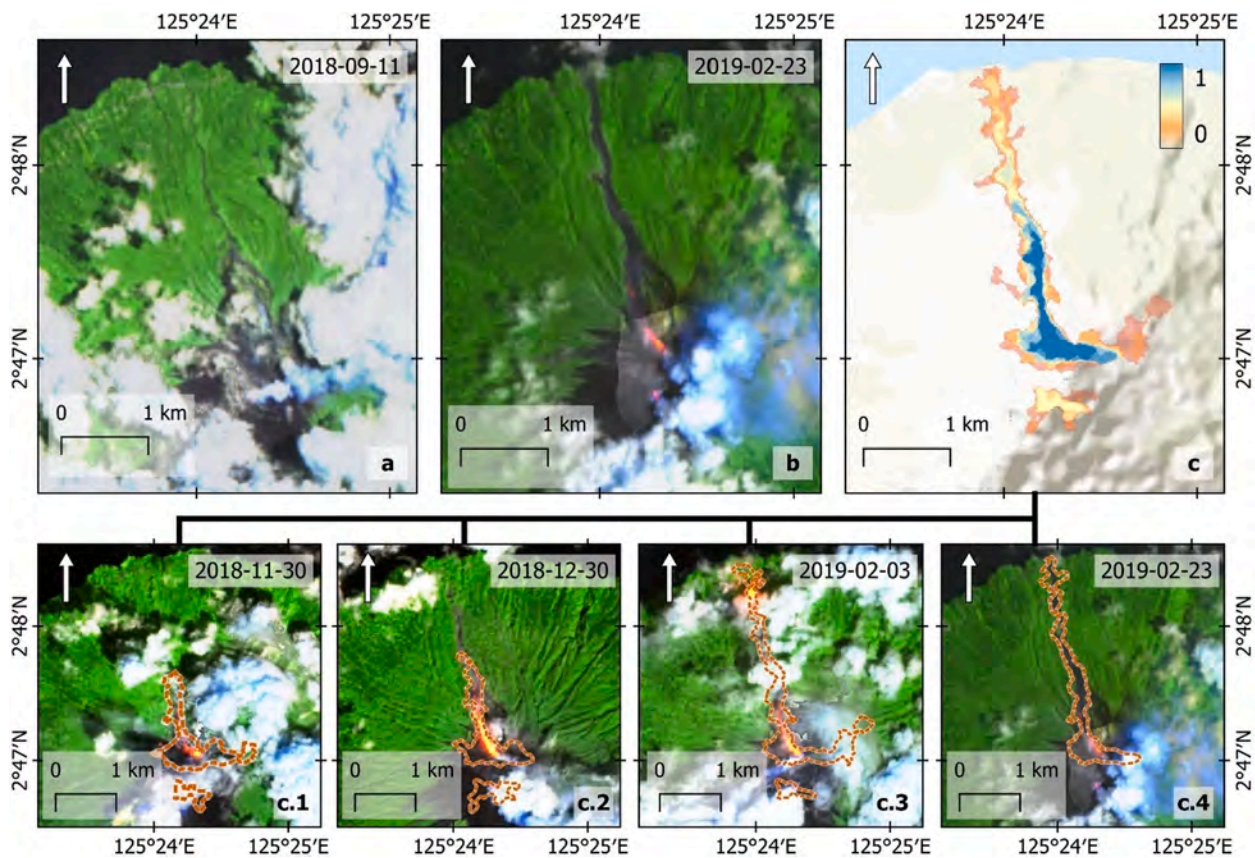


Fig. 10. Change detection results from Karangetang (N) event. Sentinel-2 (a) pre- and (b) post-event images with the (c) consistency of detected changes ranging from 1 to 0, where higher values indicate high continuity of detected changes. More detailed change maps show the spatial extent of the changes in each time step during the event (c.1, c.2, c.3, c.4). Sentinel-2 images are displayed as false colour composites (R:B12, G:B11, B:B04) where thermal anomalies are visible in red and yellow colours. (For interpretation of the references to color in this figure legend, the reader is referred to the web version of this article.)

and the size of the segments to 70x70 pixels for all runs. The segmentation was run on multivariate input consisting of NDVI composite, mNDI layers of coherence and, depending in the experimental setup, radar brightness and/or polarimetric decomposition features.

4.4. Region growing

The fundamental postulate of region growing method is that neighbouring pixels or objects within the same region have similar values, where the growing criteria is defined based on the similarity threshold. Introduced by Adams and Bischof (1994), the seeded region growing allows controlling the initial formation of the regions by providing the location of seeds. We adapted the seeded region growing mechanism to fit our application driven needs and constructed knowledge-based seeded region growing workflow (Fig. 6). The proposed workflow follows the pre-defined growth criteria based on the multivariate input data starting at automatically selected or predefined seed segments.

The region growing process is first initiated by selecting all segments where seed points lay. These segments were defined as a *candidate* segments. The region growing starts by evaluating if the *candidate* segment represents a vegetated or unvegetated area using the 'last-available-pixel' NDVI composite. Segments with median NDVI value above or equal to 0.2 are defined as a vegetated. Consequently, every pixel below the threshold was defined as unvegetated. When unvegetated, if interferometric coherence values in candidate segments were below 0.3 this segment is labelled as a *change* segment. Otherwise, the candidate segment is discarded from further evaluation and labelled as *discarded* segment. For vegetated *candidate* segments we used three groups of mNDI features: radar brightness in two polarizations (VV, VH),

polarimetric features (Alpha, Entropy and Anisotropy) and their combination. If vegetated *candidate* segment's median values at any feature in the group lies outside of two standard deviations due to a strong increase or decrease of the radar backscatter, the segment is labelled as a *change*. Otherwise, it is discarded and marked as *discarded* segment. At the end of each loop, all segments lying within 200 m buffer distance from the newly added 'change' segments are included to the 'candidate' segments list. The procedure runs until all candidate segments are being evaluated (Fig. 7).

The most critical parts of the seeded region growing is the selection of initial seeds. The speckle noise, inherently present in SAR data, often leads to the detection of false changes. Whereas, automated seed point selection using e.g. thresholding or edge detection techniques may results in detecting changes that are not directly related to the volcanic activity. To avoid this, we incorporate expert knowledge into the seed selection procedure and tailored it to our application case.

During a volcanic eruption, craters above the active vents are normally the source of the ejected materials that lead to temporal or permanent change of land surface. Due to the precursory signs or previous activity the location of active vents is typically known. Thus, as a rule of thumb the location of active vents are selected as initial seeds.

Apart from the seeds above active vents, seeds were also placed on thermal anomalies detected by the NHI algorithm, which was designed to perform on satellite data at mid-high spatial resolution (Marchese et al., 2019; Mazzeo et al., 2021). This multi-channel algorithm, running operational within the NHI tool, a GEE-App for the active volcanoes monitoring (Genzano et al., 2020; Marchese and Genzano, 2022), identifies thermal anomalies by exploiting the sensitivity of short-wave infrared (SWIR) portion of the electromagnetic spectrum to the high-

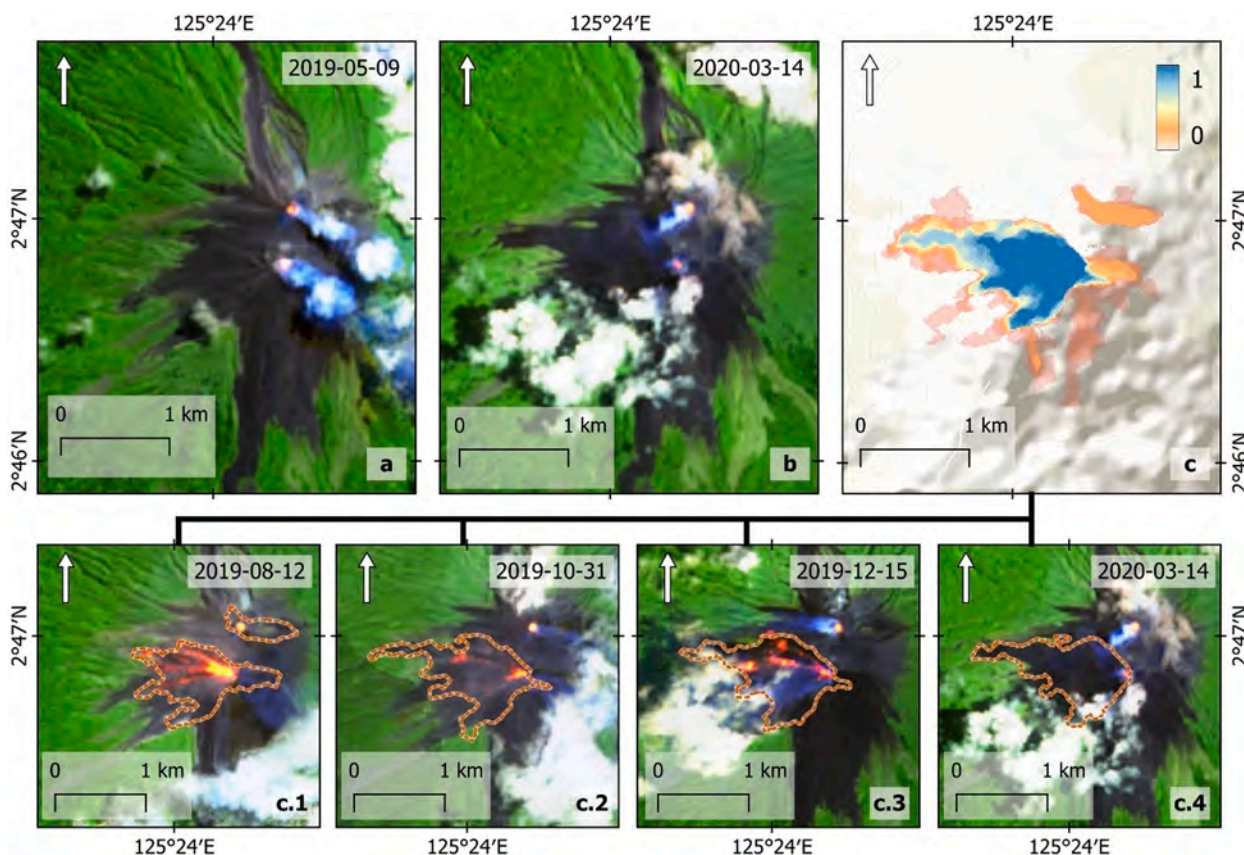


Fig. 11. Change detection results from Karangetang (W) event. Sentinel-2 (a) pre- and (b) post-event images with the (c) consistency of detected changes ranging from 1 to 0, where higher values indicate high continuity of detected changes. More detailed change maps show the spatial extent of the changes in each time step during the event (c.1, c.2, c.3, c.4). Sentinel-2 images are displayed as false colour composites (R:B12, G:B11, B:B04) where thermal anomalies are visible in red and yellow colours. (For interpretation of the references to color in this figure legend, the reader is referred to the web version of this article.)

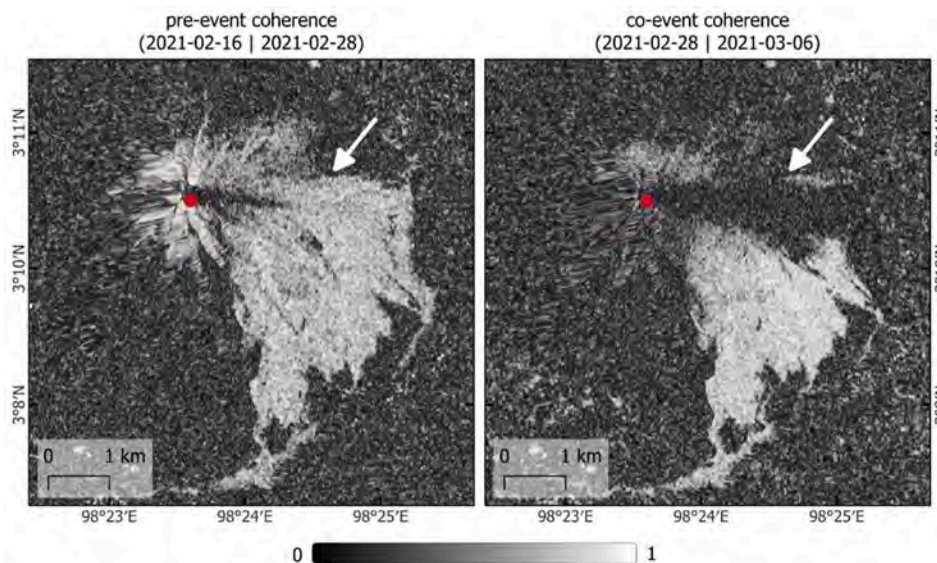


Fig. 12. Interferometric pre-event and co-event coherence of Sinabung activity of 2nd of March 2021. The red dot indicates the vent location. (For interpretation of the references to color in this figure legend, the reader is referred to the web version of this article.)

temperature features (e.g., lava flows). We used the Sentinel-2 A/B scenes acquired during the analysed volcano activity. Detected thermal anomalies were selected as seeds along additional to the initial seeds above active vents. For long time-series events, such as Karangetang (N) and Karangetang (W), the accumulative collection of the detected

thermal anomalies since the beginning of the event were used to set the seed points. The final binary output (change vs no-change) are derived after performing morphological operations such as dilation and erosion (kernel size of 3x3) on the output of region growing workflow.

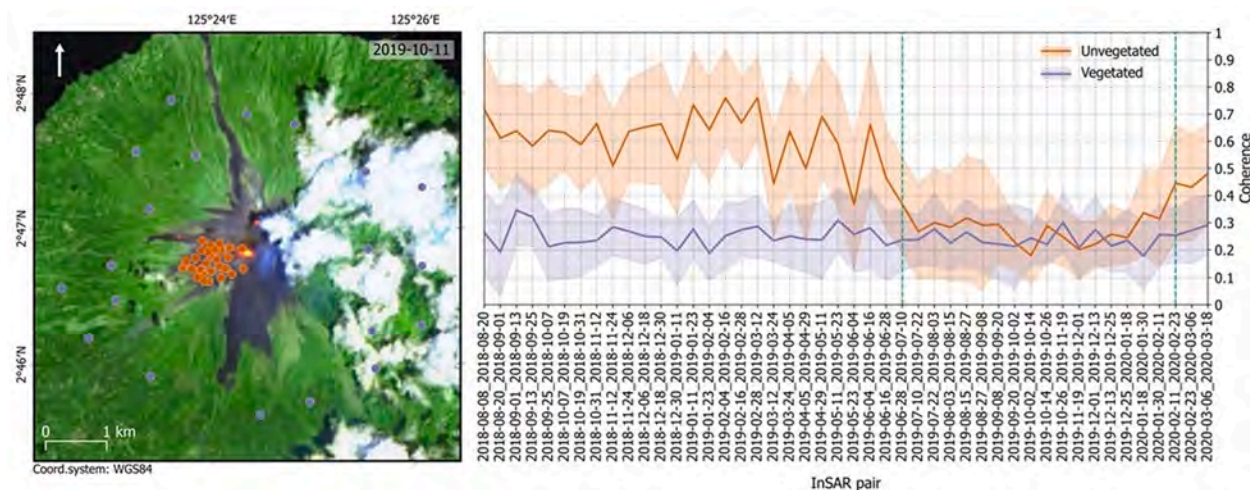


Fig. 13. Interferometric coherence time-series before and during Karangetang (W) eruption over vegetated and unvegetated surfaces.

4.5. Accuracy estimation

The accuracy of the change maps was assessed in three ways: visual evaluation, area-based and point-based accuracy assessment. In visual evaluation, we compare the change detection results with the description of the corresponding events available via various reporting sources (e.g., Global Volcanism Program, news). The area-based assessment was carried out using the reference data created by interpreting and manually digitizing the changed areas with the help of the available pre- and post-event Sentinel-2, Landsat-8 and Sentinel-1 images. We used Intersection over Union (IoU) and Dice Coefficient as area-based accuracy measures (eq. 2 and 3 accordingly).

$$IoU = \frac{\text{area of overlap}}{\text{area of union}}$$

$$Dicecoefficient = 2 \times \frac{\text{area of overlap}}{\text{total area}} \quad (3)$$

Since it is hard to obtain clear boundaries of the changed sites, the area-based accuracy assessment can have high uncertainties. The difficulty is associated with the constant presence of clouds in optical scenes, no contrast of change to the background and fuzzy border (e.g., ashfall) of the change, especially on the unvegetated flanks of the volcanoes. To obtain another quality measure we perform a point-based assessment, where 500 reference points from changed and non-changed area were sampled manually. The sites with high uncertainty were left out. Then, using total of 1000 samples from change and non-change classes we calculated F1-score measures (eq. (4)). The point-based accuracies should not be confused with pixel accuracies where the percentage of correctly classified pixels are provided. This is not based on pixels of the reference file but on randomly distributed points around the volcano that were placed in areas with high certainty of change and non-change.

$$F1score = \frac{TruePositive}{TruePositive + \frac{1}{2}(FalsePositive + FalseNegative)} \quad (4)$$

5. Results

We run the change detection workflow using only (1) radar brightness, (2) only polarimetric decomposition features and (3) their combination in order to examine the added values of polarimetric features to the change detection procedure. Also, test runs with one and five pre-event scenes for each of the above-mentioned experiments were executed. In total, the results of 30 experiments are presented and discussed in the paper.

5.1. Change detection results

The test cases considered in this study represent examples of long-term or permanent land surface change due to the simultaneous or sequential ejection of materials produced during volcanic eruptions. For example, during the eruption of Semeru volcano occurring in December 2021, pyroclastic density currents were followed by lahars. In both activities in Karangetang, the reports show that before ejection of the lava, several pyroclastic density currents were registered. Thus, the changes on the volcano flanks are the result of the cascade of events that occurred during the volcanic activity.

5.1.1. Input feature groups

The highest area-based accuracies were reached using radar brightness features for Semeru, Sinabung and for both test cases in Karangetang (Fig. 8). But, as shown in Table 3, the difference between accuracies based on only radar brightness and its combination with the polarimetric decomposition features were small (not more than + 0.06 IoU and + 0.03 Dice). Apart from Karangetang (N) case, such differences were mainly due to the slight over-estimation (false positives) of changed area on unvegetated sites very close to volcanoes' active vents. Since reference points were often not placed around volcano vents (region with high uncertainty of change), the point-based accuracies showed higher values for runs with the combination of two feature groups (Table 4). For Karangetang (N) case, over-estimation of changes occurred mainly on vegetated sites along the narrow lava flow channel. The detailed maps with area-based accuracies are provided Figs. A.2 to A.5. in appendices.

In contrast to the previous four test cases, polarimetric decomposition features alone performed better than radar brightness features in Ulwaun, where heavy ash and scoria fall was reported. The combination of both feature groups resulted in the highest area-based (Table 3) and point-based accuracies (Table 4). This is mainly due to better detection of ashfall deposits on western flank of the volcano. However, radar brightness features were able to better map the narrow path of pyroclastic density current or lahar that occurred in south-eastern site of the volcano (see Fig. A.5 in appendices). When combined, it resulted into improved detection of land surface changes due to the ashfall and pyroclastic density current or lahar.

5.1.2. Number of Pre-Event scenes

Except for Sinabung, the highest accuracies were consistently reached with mNDI features that were generated using five pre-event scenes (see, Table 3 and 4). The accuracy increase was the highest for

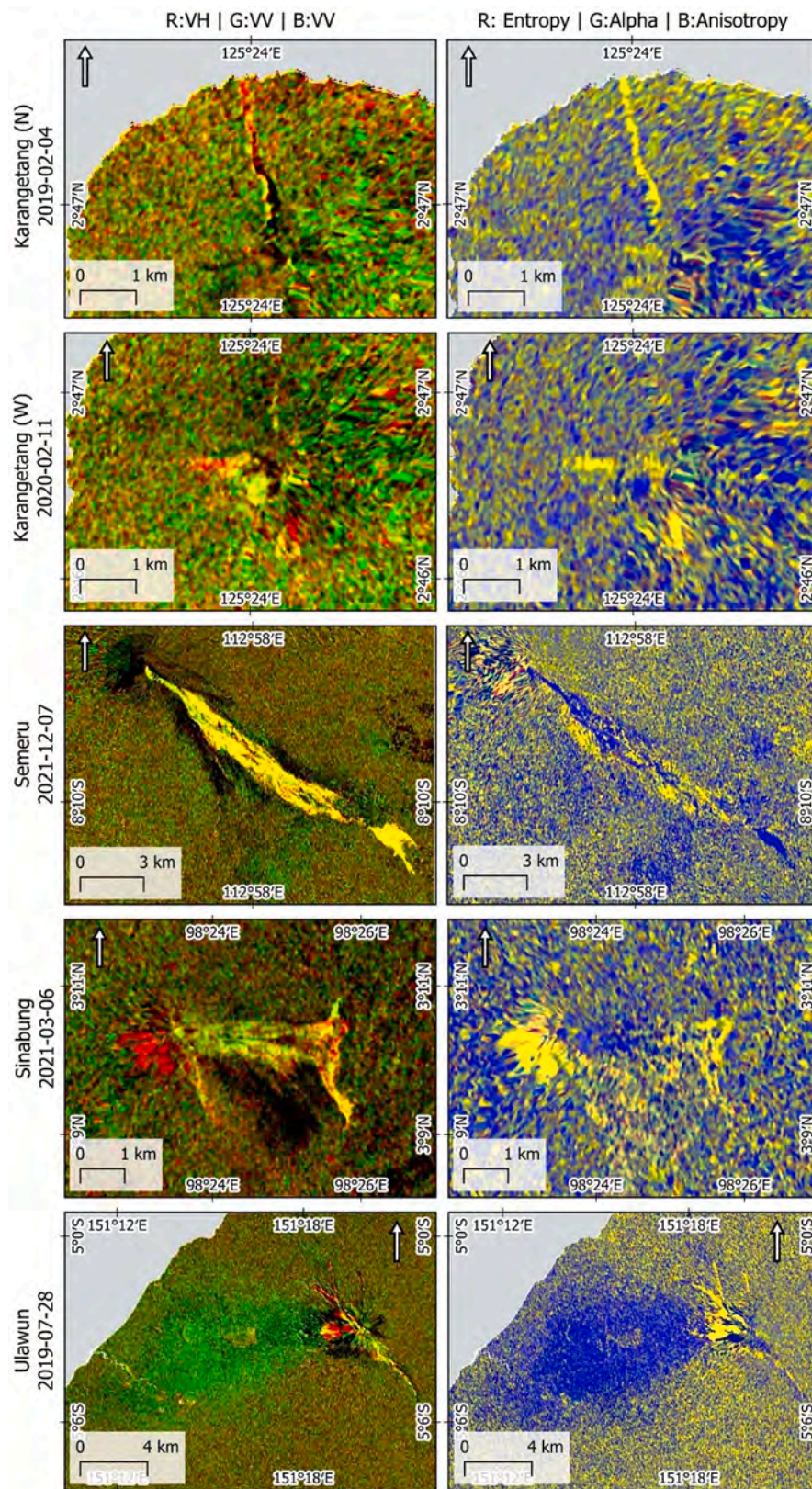


Fig. 14. RGB image composites of mNDI features from radar brightness (first column) and polarimetric decomposition layers (second column) of all five test cases (rows). Formerly vegetated areas destroyed by lava flows can clearly be seen (in yellow) on polarimetric decomposition features from Karangetang (N) and (W) events. The footprint of PDCs and lahar deposits are visible in yellow on radar brightness features from Semeru, Sinabung and Ulawun (south-eastern side) events. The regions affected by heavy ashfall appears differently on radar brightness features (light green appearance on Ulawun events and black on Sinabung and Semeru events) and polarimetric decomposition features (blue appearance on Ulawun event and yellow colour in Semeru and Sinabung events). (For interpretation of the references to color in this figure legend, the reader is referred to the web version of this article.)

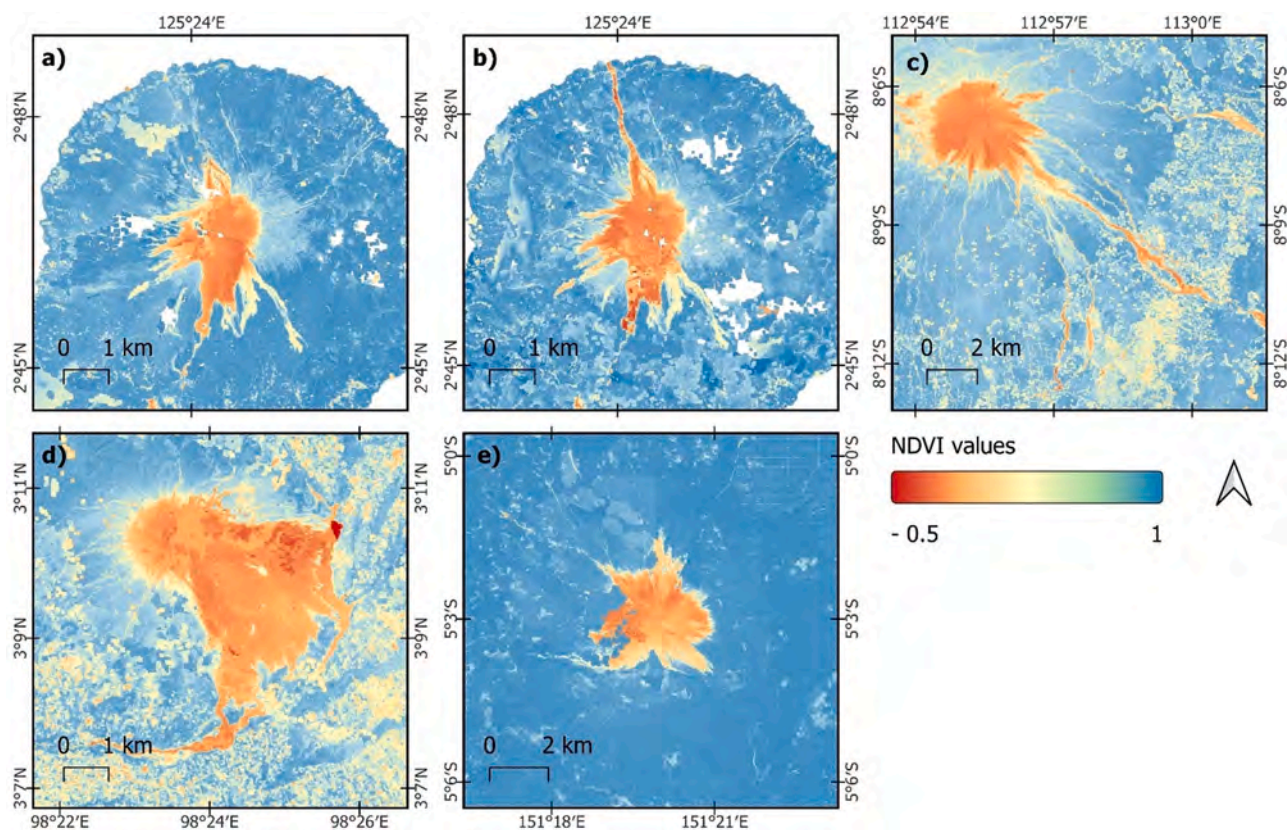


Fig. A1. The ‘last-available-pixel’ NDVI composites of a) Karangetang (N), b) Karangetang (W), c) Semeru, d) Sinabung, and e) Ulawun. White color represent ‘no data’.

Ulawun (Δ IoU + 0.10, Δ Dice + 0.10) and Karangetang (N) (Δ IoU + 0.12, Δ Dice + 0.12) when using five pre-event scenes with polarimetric decomposition features. Increasing the number of pre-event scenes helped to better detect the ashfall deposits for Ulawun and to better map the narrow lava channel in Karangetang (N). For Semeru (Fig. 9), it was possible to detect the full coverage of lahar deposits, also east of the narrow valley through the topographic ridge in the very south-eastern of Mt. Semeru (Fig. 9). For test case in Sinabung, the accuracies based on one pre-event scene were slightly better (Δ IoU + 0.02, Δ Dice + 0.01) than those based on five pre-event scenes. However, the differences of the accuracies between runs with one and five pre-event scenes are almost negligible, i.e. 0.03 for Δ IoU and Δ Dice.

5.1.3. Time-Series events in Karangetang

Two lava flow events at Karangetang Volcano lasted for several months. When testing the accuracies of the events, we used the changes detected on specific dates but also considered the reports from Global Volcanism Program (GVP) describing the events (“Global Volcanism Program,” 2022).

The changes were detected around both craters on the image from 30 of November 2018 (Fig. 10, c.1) but predominantly larger at the northern crater than at the southern one. The GVP report suggests that at the end of November 2018 after increased seismicity, lava flow extrusion occurred from the northern crater and triggered series of avalanches and pyroclastic density currents. The lava flow headed towards northern direction along the deep river channel (see, appendix A.7), which was well detected on Sentinel-2 images from December and February (Fig. 10, c.2, c.3). Closer to the end of February, lava entered the sea (Fig. 10, c.4). The consistency of detected changes (Fig. 10 c) also show that changes occurred from northern crater and moved with the time towards north.

Daily incandescent avalanche blocks were reported to be travelling on western and north western direction from mid-July 2019 until mid-January 2020 from Karangetang’s southern crater (also called as a “main crater”). The changes detected on the early stages were mainly covering unvegetated sites (Fig. 11, c.1), but in October 2019 lava entered the forested area on the western flank (Fig. 11, c.2). Ejection of incandescent avalanche blocks continued throughout the following three months, and ended approximately at the end of January 2020.

5.2. Descriptive capabilities of input features

Interferometric coherence layers were capable of capturing the changes on unvegetated sites. This can be well seen in the test case of Sinabung, where large part of the volcano’s eastern flank is unvegetated due to the previous explosive eruptions (Fig. 12). The coherence substantially drops on the unvegetated area along the reported PDCs path, where previously high coherence was observed.

Also, the time-series of coherence layers indicated the drop of coherence values to the levels of vegetated sites (Fig. 13) during the activity on Karangetang from August 2018 until March 2020. The duration of the lowered coherence values fits to the duration of reported activity on the southern (main) crater of Karangetang.

While coherence showed a good performance in detecting the changes on unvegetated sites, mapping of the changes on vegetated sites were more complex with SAR data. Among all the tested features, radar brightness features were best capable of showing narrow structural changes on volcanic flanks (Fig. 14). Yet, polarimetric decomposition features shows better the changes due to the heavy ashfall.

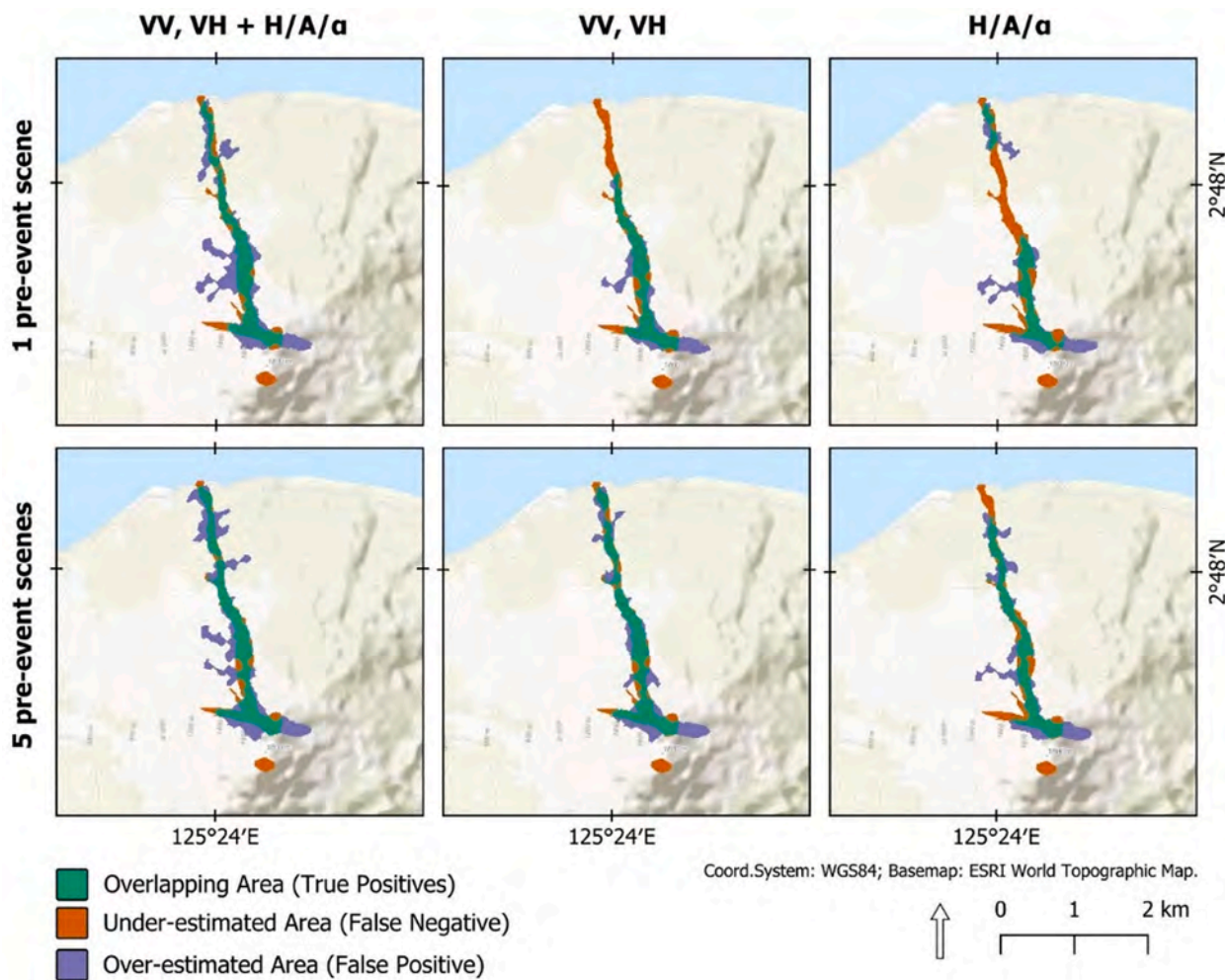


Fig. A2. Area-based change detection results using three features groups (columns) calculated based on one and five pre-event scenes (rows) in Karangetang (N).

6. Discussion

In this paper, we propose a semi-automated unsupervised, knowledge-based seeded region growing procedure for land surface change detection after volcanic eruptions based on freely available SAR data from Sentinel-1 supported by optical data from Sentinel-2. The method, based on five test cases in Indonesia and Papua New Guinea, showed promising results in detecting changes using the first available post-event Sentinel-1 data. Usage of freely available remote sensing datasets within the workflow supports the reproducibility of the method, by removing the constraints associated with data acquisitions costs.

Radar brightness features alone with interferometric coherence data was enough to detect the changes at the acceptable accuracy in all test cases except for Ulawun. Similar results were reported in the previous studies (Bignami et al., 2020; Smets et al., 2010; Solikhin et al., 2015). Complementary to the existing knowledge, we found that addition of polarimetric decomposition features improves the discrimination of heavy ashfall deposits. The combination of radar brightness and polarimetric decomposition features could improve the change detection accuracy in such complex eruption cases as Ulawun.

Using five pre-event scenes instead of only one allowed to better delineate the destruction of vegetation cover caused by volcanic activities. This consequently resulted in higher change detection accuracies. Such accuracy improvements could be due to the elimination of the random amplitude fluctuations that are not related to the changes from the target event. However, when most of the affected area is unvegetated, as it is in the Sinabung example, increasing the number of pre-event scenes has almost no impact on the change accuracies.

As for any seeded region growing procedure, the initial location of seeds has a substantial effect on the quality of the output change mask. The results from Sinabung and Semeru, where thermal anomalies were detected only around the crater, have illustrated that the presented approach is capable of delivering promising results even with the few initial seeds on the crater and in its close surroundings. However, inclusion of detected thermal anomalies as seed point substantially facilitated the multi-temporal change detection in both eruption events in Karangetang. Addition of thermal anomaly information into the workflow could also assist if new vent opening occurs, as recently happened in La Palma (Canary Islands) end of 2021 (Walter et al. in press).

The presented change detection method is an unsupervised method, as the majority of approaches presented in the literature on the subject.

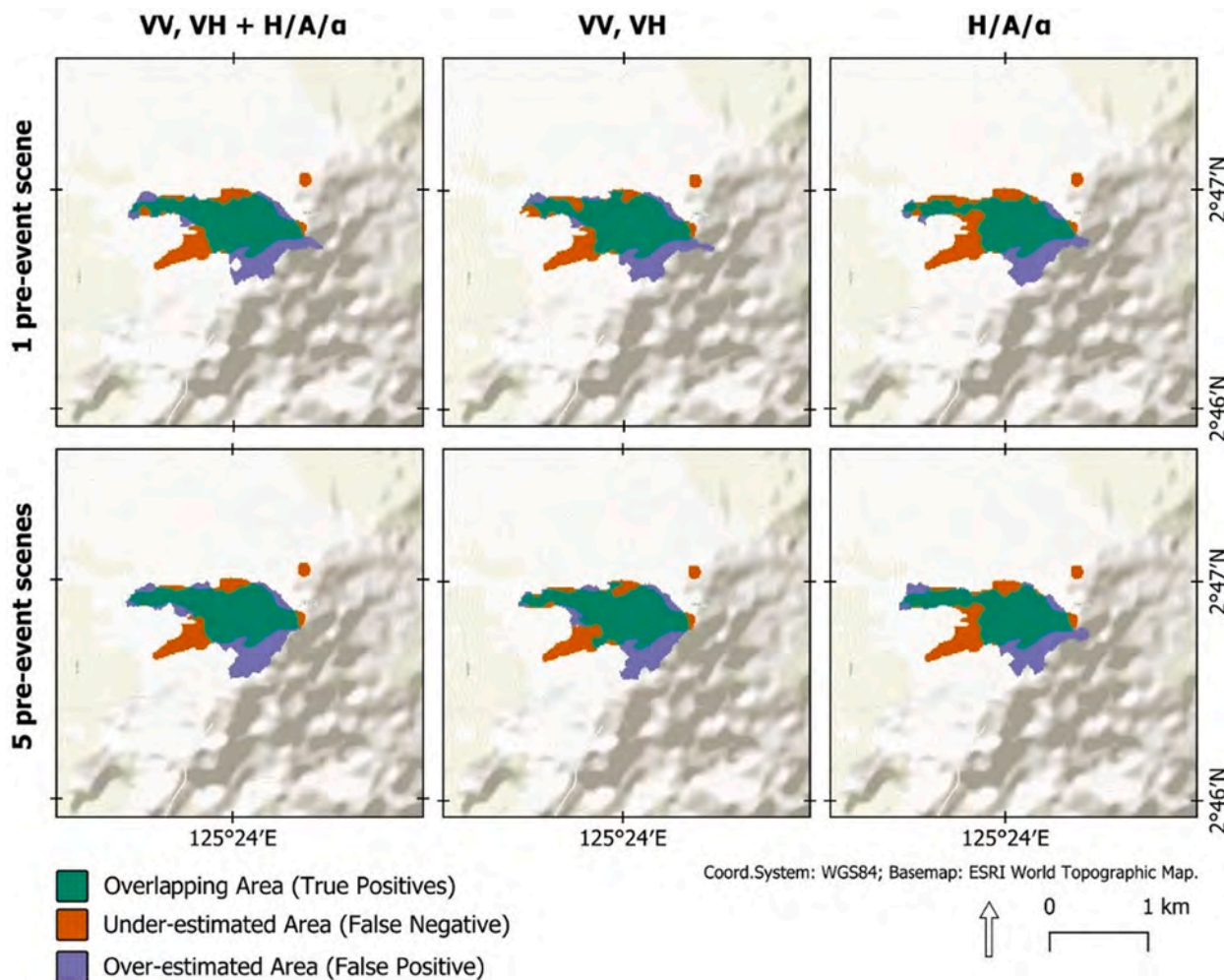


Fig. A3. Area-based change detection results using three features groups (columns) calculated based on one and five pre-event scenes (rows) in Karangetang (W).

The absence of representative reference data, which are required for training the machine learning models, are among the main reasons for domination of unsupervised approaches over supervised once. Additionally, in case of ashfall or PDCs, defining the spatial boundaries of ‘change’ is challenging due to the gradual fading of the ‘change’. In such cases, spatial border of effected sites may vary depending on the decision of each individual. Despite these challenges, recently published papers on supervised classification of volcanic deposits (e.g., Corradino et al., 2021, 2019) illustrate the growing effort to move towards supervised machine learning solutions.

In future, further developments should aim to overcome following limiting factors of the current version of the presented algorithm. Firstly, NDVI ‘last-available-pixel’ composite may inherit a short-term pre-eruption vegetation disturbance, which result in false assignment of the segment to unvegetated region. Additionally, the quality of the composite heavily relies on the quality of the used cloud masks. Secondly, due to its side-looking image acquisition geometry, SAR data may contain substantial image artefacts that could be detected as change (e.g. Karangetang (N)). In complex topographic conditions, the continuity of the signal alteration due to the real change could be disrupted (e.g. Semeru). Thirdly, segments overlapping inland water bodies should be

filtered out since there segments would be marked as change when considered by region growing rules. Currently, the workflow consists of separately executed three modules. One of the priority future objective is to move from semi-automated to fully automated procedure that could require only information on volcano location and event dates.

7. Conclusions and outlook

Volcano induced hazards are one of the major threats to densely populated communities around active volcanoes. When volcanic eruption occurs, the timely delivered information on impacted areas is critical. This study presents a semi-automated approach on land surface change detection after volcanic eruptions and examines the added value of polarimetric decomposition features and increased number of pre-event SAR scenes to the change detection accuracies.

The proposed semi-automatic change detection method showed promising results for all five eruption cases that considerably differ from each other by their spatial extent, duration of eruption, topography of affected sites and volcanic deposits that caused the land surface change. The workflow jointly utilizes freely available Sentinel-1 and Sentinel-2 data. With the consistent pattern across all test cases, we illustrated

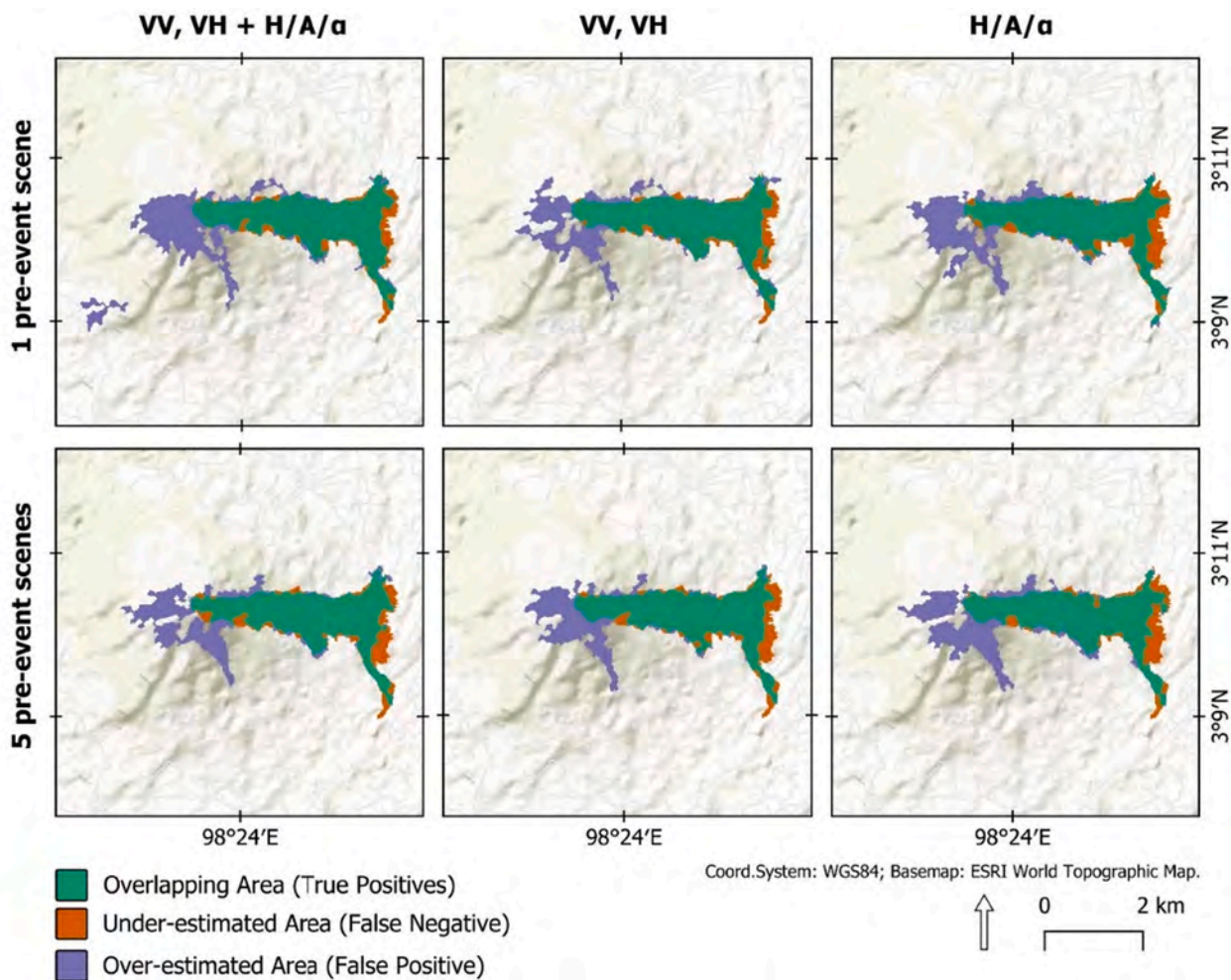


Fig. A4. Area-based change detection results using three features groups (columns) calculated based on one and five pre-event scenes (rows) in Sinabung.

that using more than one pre-event SAR scene for calculating mNDI features helps to improve the change detection accuracies. Also, addition of polarimetric decomposition features improves mapping of ashfall deposits (e.g., Ulawun). However, in test cases where no heavy ashfall was reported usage of only radar brightness data in vegetated sites was enough to reach the maximum accuracies.

In the future, we consider including post-event cloud-free and cloud-shadow-free optical data to enhance the detection of changes in vegetated regions. This implies that the decision on segment’s status would not be purely based on SAR data but also on optical, if available. Also, instead of defining a concrete buffer size for searching candidate segments, a self-adjustable scheme should be implemented that is positively correlated with the topographic complexity of the area. With the increasing topographic complexity, the buffer size should increase (to avoid stopping the workflow due to the increased geometric distortions present in SAR) and vice versa if complexity decreases (to avoid inclusion of too many candidate segments that slows down the process).

The change detection workflow is specifically tailored to the volcanoes in Southeast Asia, where volcano flanks are typically densely vegetated. However, it can be adjusted to other volcanic regions where the separation between two or more land cover classes (e.g., snow, bare soil and vegetation) could be of interest.

Funding

Financial support by the Client II Project Tsunami_Risk (BMBF Funding reference number 03G0906B) is acknowledged.

CRediT authorship contribution statement

Aiym Orynbaikyzy: Conceptualization, Methodology, Writing – original draft, Writing – review & editing. **Simon Plank:** Conceptualization, Methodology, Writing – original draft, Writing – review & editing. **Yenni Vetrita:** Resources, Writing – review & editing. **Sandro Martinis:** Funding acquisition, Supervision, Writing – review & editing. **Imam Santoso:** Writing – review & editing. **Rido Dwi Ismanto:** Writing – review & editing. **Farikhotul Chusnayah:** Writing – review & editing. **Arum Tjahjaningsih:** Writing – review & editing. **Suwarsono:** Writing – review & editing. **Nicola Genzano:** Resources, Writing – review & editing. **Francesco Marchese:** Resources, Writing – review & editing. **M. Rokhis Khomarudin:** Writing – review & editing. **Günter Strunz:** Funding acquisition, Supervision, Writing – review & editing.

Declaration of Competing Interest

The authors declare that they have no known competing financial interests or personal relationships that could have appeared to influence the work reported in this paper.

Data availability

Data will be made available on request.

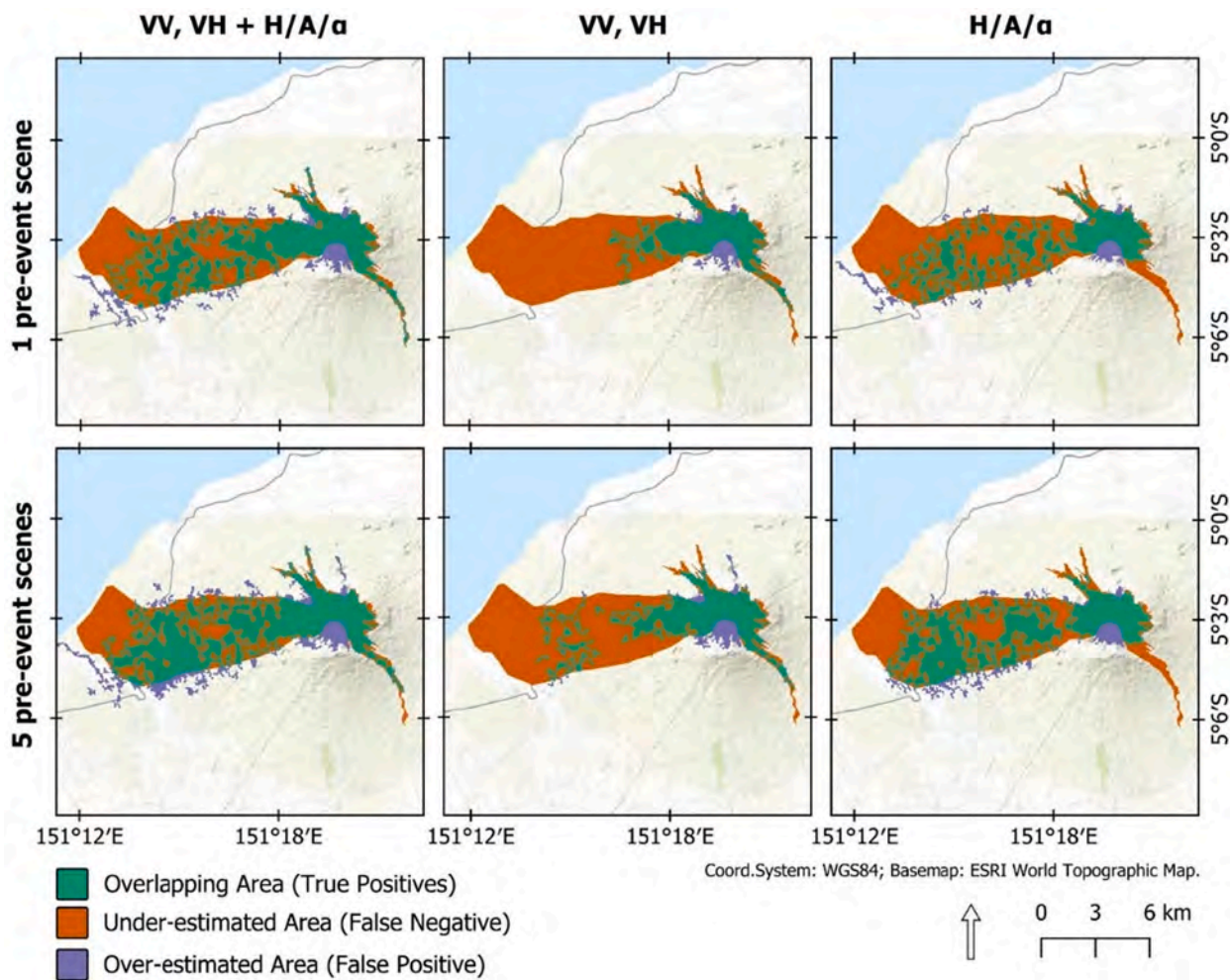


Fig. A5. Area-based change detection results using three features groups (columns) calculated based on one and five pre-event scenes in Ulawun.

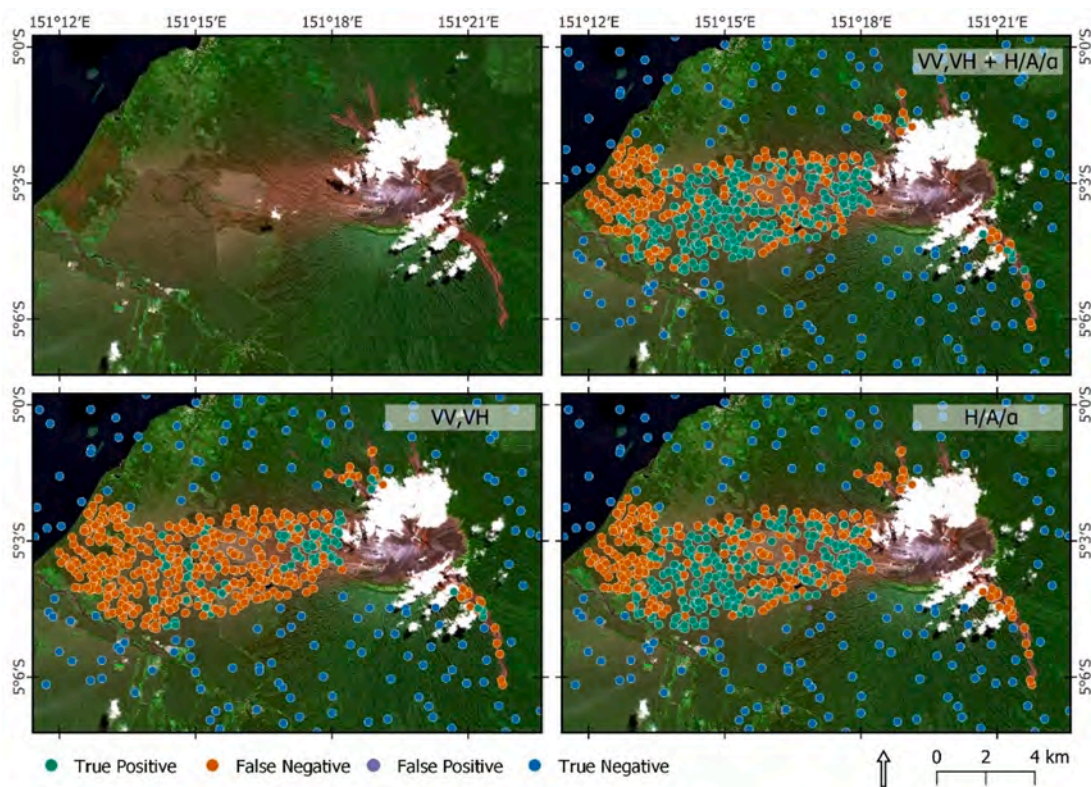


Fig. A6. Point-based change detection results using three features groups calculated using five pre-event scenes in Ulawun.



Fig. A7. The image from lava field on northern flank occurred due to Karangetang (N) event. Image taken on 23rd of August 2022.

Appendix

See Figs. A1–A7.

References

- Achanta, R., Shaji, A., Smith, K., Lucchi, A., Fua, P., Süsstrunk, S., 2012. SLIC Superpixels Compared to State-of-the-Art Superpixel Methods. *IEEE Trans. Pattern Anal. Mach. Intell.* 34, 2274–2282. <https://doi.org/10.1109/TPAMI.2012.120>.
- Adams, R., Bischof, L., 1994. Seeded region growing. *IEEE Trans. Pattern Anal. Machine Intell.* 16, 641–647. <https://doi.org/10.1109/34.295913>.
- Aldeghi, Carn, Escobar-Wolf, Gropelli, 2019. Volcano Monitoring from Space Using High-Cadence Planet CubeSat Images Applied to Fuego Volcano. *Guatemala. Remote Sensing* 11 (18), 2151.
- Auker, M.R., Sparks, R.S.J., Siebert, L., Croweller, H.S., Ewert, J., 2013. A statistical analysis of the global historical volcanic fatalities record. *J Appl. Volcanol.* 2, 2. <https://doi.org/10.1186/2191-5040-2-2>.
- Barclay, J., Few, R., Armijos, M.T., Phillips, J.C., Pyle, D.M., Hicks, A., Brown, S.K., Robertson, R.E.A., 2019. Livelihoods, Wellbeing and the Risk to Life During Volcanic Eruptions. *Front. Earth Sci.* 7, 205. <https://doi.org/10.3389/feart.2019.00205>.
- Bevege, A., 2019. Papua New Guinea volcanic eruptions force 15,000 from their homes. <https://www.reuters.com/article/us-papua-volcano/papua-new-guinea-volcanic-eruptions-force-15000-from-their-homes-idUSKCN1TV07R>.
- Bigname, C., Chini, M., Amici, S., Trasatti, E., 2020. Synergic Use of Multi-Sensor Satellite Data for Volcanic Hazards Monitoring: The Fogo (Cape Verde) 2014–2015 Effusive Eruption. *Front. Earth Sci.* 8, 22. <https://doi.org/10.3389/feart.2020.00022>.
- Braaten, J., 2022. Sentinel-2 Cloud Masking with s2cloudless. *Google Earth Engine Community*. URL <https://developers.google.com/earth-engine/tutorials/community/sentinel-2-s2cloudless> (accessed 7.5.22).
- Brisco, B., Schmitt, A., Mumaghan, K., Kaya, S., Roth, A., 2013. SAR polarimetric change detection for flooded vegetation. *International Journal of Digital Earth* 6, 103–114. <https://doi.org/10.1080/17538947.2011.608813>.
- Cigna, F., Tapete, D., Lu, Z., 2020. Remote Sensing of Volcanic Processes and Risk. *Remote Sensing* 12, 2567. <https://doi.org/10.3390/rs12162567>.
- Clauss, K., Ottinger, M., Kuenzer, C., 2018. Mapping rice areas with Sentinel-1 time series and superpixel segmentation. *International Journal of Remote Sensing* 39, 1399–1420. <https://doi.org/10.1080/01431161.2017.1404162>.
- Cloude, S.R., Pottier, E., 1997. An entropy based classification scheme for land applications of polarimetric SAR. *IEEE Trans. Geosci. Remote Sensing* 35, 68–78. <https://doi.org/10.1109/36.551935>.
- Corradino, C., Ganci, G., Cappello, A., Bilotta, G., Hérault, A., Del Negro, C., 2019. Mapping Recent Lava Flows at Mount Etna Using Multispectral Sentinel-2 Images and Machine Learning Techniques. *Remote Sensing* 11, 1916. <https://doi.org/10.3390/rs11161916>.
- Corradino, C., Bilotta, G., Cappello, A., Fortuna, L., Del Negro, C., 2021. Combining Radar and Optical Satellite Imagery with Machine Learning to Map Lava Flows at Mount Etna and Fogo Island. *Energies* 14, 197. <https://doi.org/10.3390/en14010197>.
- De Beni, E., Cantarero, M., Neri, M., Messina, A., 2021. Lava flows of Mt Etna, Italy: the 2019 eruption within the context of the last two decades (1999–2019). *Journal of Maps* 17, 65–76. <https://doi.org/10.1080/17445647.2020.1854131>.
- Dietterich, H.R., Poland, M.P., Schmidt, D.A., Cashman, K.V., Sherrod, D.R., Espinosa, A. T., 2012. Tracking lava flow emplacement on the east rift zone of Kilauea, Hawai'i, with synthetic aperture radar coherence. *Geochem. Geophys. Geosyst.* 13, Q05001. <https://doi.org/10.1029/2011GC004016>.
- Genzano, N., Pergola, N., Marchese, F., 2020. A Google Earth Engine Tool to Investigate, Map and Monitor Volcanic Thermal Anomalies at Global Scale by Means of Mid-High Spatial Resolution Satellite Data. *Remote Sensing* 12, 3232. <https://doi.org/10.3390/rs12193232>.
- Global Volcanism Program, 2019a. Report on Karangetang (Indonesia) (Krippner, J.B., and Venzke, E., eds.), *Bulletin of the Global Volcanism Network*, 44:5. Smithsonian Institution. <https://doi.org/10.5479/si.GVP.BGVN201905-267020>.
- Global Volcanism Program, 2019b. Report on Ulawun (Papua New Guinea) (Venzke, E., ed.), *Bulletin of the Global Volcanism Network*, 44:9. Smithsonian Institution. <https://doi.org/10.5479/si.GVP.BGVN201909-252120>.
- Global Volcanism Program, 2020. Report on Karangetang (Indonesia) (Crafford, A.E., and Venzke, E., eds.), *Bulletin of the Global Volcanism Network*, 45:6. Smithsonian Institution. <https://doi.org/10.5479/si.GVP.BGVN201905-267020>.
- Global Volcanism Program, 2021. Report on Sinabung (Indonesia) (Crafford, A.E., and Venzke, E., eds.), *Bulletin of the Global Volcanism Network*, 46:8. Smithsonian Institution. <https://doi.org/10.5479/si.GVP.BGVN202108-261080>.
- Global Volcanism Program, 2022. Report on Semeru (Indonesia) (Crafford, A.E., and Venzke, E., eds.), *Bulletin of the Global Volcanism Network*, 47:1. Smithsonian Institution.
- Global Volcanism Program [WWW Document], 2022. . Smithsonian Institution, National Museum of Natural History, Global Volcanism Program. URL <https://volcano.si.edu/> (accessed 9.12.22).
- Gorelick, N., Hancher, M., Dixon, M., Ilyushchenko, S., Thau, D., Moore, R., 2017. Google Earth Engine: Planetary-scale geospatial analysis for everyone. *Remote Sensing of Environment* 202, 18–27. <https://doi.org/10.1016/j.rse.2017.06.031>.
- Handley, H., 2021. Mount Semeru's deadly eruption was triggered by rain and storms, making it much harder to predict [WWW Document]. accessed 12.5.22 The Conversation. <https://theconversation.com/mount-semerus-deadly-eruption-was-triggered-by-rain-and-storms-making-it-much-harder-to-predict-173240>.
- Hechteljen, A., Thonfeld, F., Menz, G., 2014. Recent Advances in Remote Sensing Change Detection – A Review. In: Manakos, I., Braun, M. (Eds.), *Land Use and Land Cover Mapping in Europe, Remote Sensing and Digital Image Processing*. Springer, Netherlands, Dordrecht, pp. 145–178. https://doi.org/10.1007/978-94-007-7969-3_10.
- Joyce, K.E., Samsonov, S., Manville, V., Jongens, R., Graettinger, A., Cronin, S.J., 2009. Remote sensing data types and techniques for lahar path detection: A case study at Mt Ruapehu, New Zealand. *Remote Sensing of Environment* 113, 1778–1786. <https://doi.org/10.1016/j.rse.2009.04.001>.
- Jung, J., Kim, D., Lavalley, M., Yun, S.-H., 2016. Coherent Change Detection Using InSAR Temporal Decorrelation Model: A Case Study for Volcanic Ash Detection. *IEEE Trans. Geosci. Remote Sensing* 54, 5765–5775. <https://doi.org/10.1109/TGRS.2016.2572166>.
- López-Puigdollers, D., Mateo-García, G., Gómez-Chova, L., 2021. Benchmarking Deep Learning Models for Cloud Detection in Landsat-8 and Sentinel-2 Images. *Remote Sensing* 13, 992. <https://doi.org/10.3390/rs13050992>.
- Mani, L., Tzachor, A., Cole, P., 2021. Global catastrophic risk from lower magnitude volcanic eruptions. *Nat Commun* 12, 4756. <https://doi.org/10.1038/s41467-021-25021-8>.
- Marchese, F., Genzano, N., 2022. Global volcano monitoring through the NHI (Normalized Hotspot Indices) system. *Journal of the Geological Society* 0, jgs2022-014. <https://doi.org/10.1144/jgs2022-014>.
- Marchese, F., Genzano, N., Neri, M., Falconieri, A., Mazzeo, G., Pergola, N., 2019. A Multi-Channel Algorithm for Mapping Volcanic Thermal Anomalies by Means of Sentinel-2 MSI and Landsat-8 OLI Data. *Remote Sensing* 11, 2876. <https://doi.org/10.3390/rs11232876>.
- Marconini, M., Metz-Marconcini, A., Esch, T., Gorelick, N., 2021. Understanding Current Trends in Global Urbanisation - The World Settlement Footprint Suite. *giferom* 1, 33–38. https://doi.org/10.1553/giscience2021_01_s33.
- Nielsen, A.A., Canty, M.J., Skriver, H., Conradson, K., 2017. Change detection in multi-temporal dual polarization Sentinel-1 data, in: 2017 IEEE International Geoscience and Remote Sensing Symposium (IGARSS). IEEE, Fort Worth, TX, pp. 3901–3908. <https://doi.org/10.1109/IGARSS.2017.8127854>.
- Mazzeo, G., Ramsey, M.S., Marchese, F., Genzano, N., Pergola, N., 2021. Implementation of the NHI (Normalized Hot Spot Indices) Algorithm on Infrared ASTER Data: Results and Future Perspectives. *Sensors* 21, 1538. <https://doi.org/10.3390/s21041538>.
- Pallister, J., Wessels, R., Griswold, J., McCausland, W., Kartadinata, N., Gunawan, H., Budianto, A., Primulyana, S., 2019. Monitoring, forecasting collapse events, and mapping pyroclastic deposits at Sinabung volcano with satellite imagery. *Journal of Volcanology and Geothermal Research* 382, 149–163. <https://doi.org/10.1016/j.jvolgeores.2018.05.012>.
- Pan, H., Shi, P., Ye, T., Xu, W., Wang, J., 2015. Mapping the expected annual fatality risk of volcano on a global scale. *International Journal of Disaster Risk Reduction* 13, 52–60. <https://doi.org/10.1016/j.ijdrr.2015.03.004>.
- Plank, S., Twele, A., Martinis, S., 2016. Landslide Mapping in Vegetated Areas Using Change Detection Based on Optical and Polarimetric SAR Data. *Remote Sensing* 8, 307. <https://doi.org/10.3390/rs8040307>.
- Rösch, M., Plank, S., 2022. Detailed Mapping of Lava and Ash Deposits at Indonesian Volcanoes by Means of VHR PlanetScope Change Detection. *Remote Sensing* 14, 1168. <https://doi.org/10.3390/rs14051168>.
- Smets, B., Wauthier, C., d'Oreye, N., 2010. A new map of the lava flow field of Nyamulagira (D.R. Congo) from satellite imagery. *Journal of African Earth Sciences* 58, 778–786. <https://doi.org/10.1016/j.jafrearsci.2010.07.005>.
- Solikhin, A., Pinel, V., Vandemeulebrouck, J., Thouret, J.-C., Hendrasto, M., 2015. Mapping the 2010 Merapi pyroclastic deposits using dual-polarization Synthetic Aperture Radar (SAR) data. *Remote Sensing of Environment* 158, 180–192. <https://doi.org/10.1016/j.rse.2014.11.002>.
- Tzouvaras, M., Danezis, C., Hadjimitsis, D.G., 2020. Small Scale Landslide Detection Using Sentinel-1 Interferometric SAR Coherence. *Remote Sensing* 12, 1560. <https://doi.org/10.3390/rs12101560>.

van der Walt, S., Schönberger, J.L., Nunez-Iglesias, J., Boulogne, F., Warner, J.D., Yager, N., Gouillart, E., Yu, T., 2014. scikit-image: image processing in Python. *PeerJ* 2, e453.

Walter, T.R., Zorn, E.U., Gonzalez, P.J., Sansosti, E., Muñoz, V., Shevchenko, A.V., Plank, S., Reale, D., Richter, N 2022. (in press): Late complex tensile fracturing interacts with topography at Cumbre Vieja, La Palma. *Volcanica*.

Wright, R., Flynn, L.P., Garbeil, H., Harris, A.J.L., Pilger, E., 2004. MODVOLC: near-real-time thermal monitoring of global volcanism. *Journal of Volcanology and Geothermal Research* 135, 29–49. <https://doi.org/10.1016/j.jvolgeores.2003.12.008>.